

THE NATURE OF INFRARED EMISSION IN THE LOCAL GROUP DWARF GALAXY NGC 6822 AS REVEALED BY *SPITZER*

JOHN M. CANNON^{1,2}, FABIAN WALTER², LEE ARMUS³, GEORGE J. BENDO^{4,5}, DANIELA CALZETTI⁶, BRUCE T. DRAINE⁷, CHARLES W. ENGELBRACHT⁵, GEORGE HELOU³, ROBERT C. KENNICUTT, JR.^{8,5}, CLAUD LEITHERER⁶, HÉLÈNE ROUSSEL², CAROLINE BOT³, BRENT BUCKALEW³, DANIEL A. DALE⁹, W. J. G. DE BLOK¹⁰, KARL D. GORDON⁵, DAVID J. HOLLENBACH¹¹, THOMAS H. JARRETT³, MARTIN J. MEYER⁶, ERIC J. MURPHY¹², KARTIK SHETH³, MICHELE D. THORNLEY¹³

Accepted for publication in the Astrophysical Journal

ABSTRACT

We present *Spitzer* imaging of the metal-deficient ($Z \simeq 30\% Z_{\odot}$) Local Group dwarf galaxy NGC 6822. On spatial scales of ~ 130 pc, we study the nature of IR, H α , H I, and radio continuum emission. Nebular emission strength correlates with IR surface brightness; however, roughly half of the IR emission is associated with diffuse regions not luminous at H α (as found in previous studies). The global ratio of dust to H I gas in the ISM, while uncertain at the factor of ~ 2 level, is ~ 25 times lower than the global values derived for spiral galaxies using similar modeling techniques; localized ratios of dust to H I gas are about a factor of five higher than the global value in NGC 6822. There are strong variations (factors of ~ 10) in the relative ratios of H α and IR flux throughout the central disk; the low dust content of NGC 6822 is likely responsible for the different H α /IR ratios compared to those found in more metal-rich environments. The H α and IR emission is associated with high-column density ($\gtrsim 10^{21}$ cm⁻²) neutral gas. Increases in IR surface brightness appear to be affected by both increased radiation field strength and increased local gas density. Individual regions and the galaxy as a whole fall within the observed scatter of recent high-resolution studies of the radio-far IR correlation in nearby spiral galaxies; this is likely the result of depleted radio and far-IR emission strengths in the ISM of this dwarf galaxy.

Subject headings: galaxies: dwarf — galaxies: irregular — galaxies: ISM — galaxies: individual (NGC 6822) — infrared: galaxies

1. INTRODUCTION

Nearby dwarf galaxies provide a unique opportunity to resolve the interaction of the multiple phases of the interstellar medium (ISM). Star formation in these systems

is more susceptible to small-scale processes (e.g., turbulence, feedback) than to the galaxy-wide perturbations (i.e., spiral density waves) that are common in more massive galaxies. With their typically low nebular metallicities, star-forming dwarf galaxies serve as fiducial examples for comparison with the high-redshift star-forming systems predicted in the cold dark matter paradigm (e.g., Babul & Ferguson 1996; Ellis 1997; Mateo 1998).

The detailed processes of heating and cooling of the ISM are fundamental to our understanding of the nature of galaxy evolution. An environmentally-dependent fraction of UV photons produced by massive stars will be absorbed by dust and gas and re-radiated in the far-infrared (FIR) or in nebular emission lines. This fraction will depend on various factors, including the local dust-to-gas ratio (related to the metallicity and hence the dust content) and the porosity of the local ISM. In cases where the dust and stars are well mixed, and where the extinction is moderate, there will exist a correlation between the fluxes in various wavelength bands, including the ultraviolet (UV), H α , FIR, and radio continuum. Nearby dwarf galaxies offer a unique opportunity to study one of the regimes where these correlations may begin to break down.

NGC 6822 is a Local Group ($D = 490 \pm 40$ kpc; Mateo 1998) dwarf irregular galaxy with a nebular abundance $Z \simeq 30\% Z_{\odot}$ (Skillman et al. 1989; Lee et al. 2006a). The total optical luminosity is $\sim 9.4 \times 10^7 L_{\odot}$ (Mateo 1998), while the total H I mass is $1.34 \times 10^8 M_{\odot}$ (see detailed discussion in § 2.2 and de Blok & Walter 2006). The system contains distributed low-level star forma-

¹ Astronomy Department, Wesleyan University, Middletown, CT 06457; cannon@astro.wesleyan.edu

² Max-Planck-Institut für Astronomie, Königstuhl 17, D-69117, Heidelberg, Germany; walter@mpia.de, rousset@mpia.de

³ California Institute of Technology, MC 314-6, Pasadena, CA 91101; lee@ipac.caltech.edu, gxb@ipac.caltech.edu, bot@caltech.edu, brentb@ipac.caltech.edu, jarrett@ipac.caltech.edu, kartik@astro.caltech.edu

⁴ Astrophysics Group, Imperial College, Blackett Laboratory, Prince Consort Road, London SW7 2AZ United Kingdom; g.bendo@imperial.ac.uk

⁵ Steward Observatory, University of Arizona, 933 North Cherry Avenue, Tucson, AZ 85721; chad@as.arizona.edu, kgordon@as.arizona.edu

⁶ Space Telescope Science Institute, 3700 San Martin Drive, Baltimore, MD 21218; calzetti@stsci.edu, leitherer@stsci.edu, martinm@stsci.edu

⁷ Princeton University Observatory, Peyton Hall, Princeton, NJ 08544; draine@astro.princeton.edu

⁸ Institute of Astronomy, University of Cambridge, Madingley Road, Cambridge CB3 0HA, UK; robk@ast.cam.ac.uk

⁹ Department of Physics and Astronomy, University of Wyoming, Laramie, WY 82071; ddale@uwyo.edu

¹⁰ Research School of Astronomy & Astrophysics, Mount Stromlo Observatory, Cotter Road, Weston ACT 2611, Australia; edeblok@mso.anu.edu.au

¹¹ NASA/Ames Research Center, MS 245-6, Moffett Field, CA, 94035; hollenba@ism.arc.nasa.gov

¹² Department of Astronomy, Yale University, New Haven, CT 06520; murphy@astro.yale.edu

¹³ Department of Physics and Astronomy, Bucknell University, Lewisburg, PA 17837; mthornle@bucknell.edu

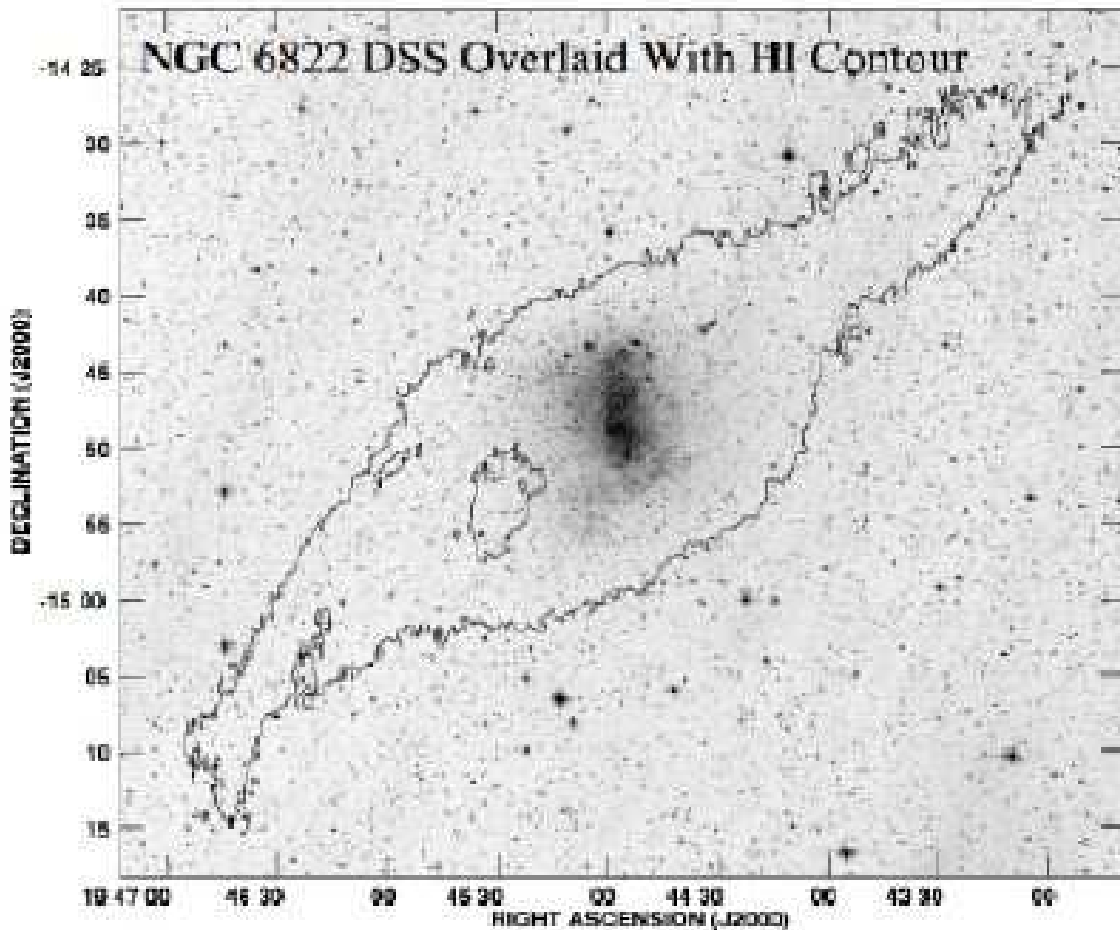


FIG. 1.— DSS image of NGC 6822, overlaid with a contour of H I column density at the $2 \times 10^{20} \text{ cm}^{-2}$ level. The H I disk is much larger than the high surface brightness optical body, which was the target of our IRAC and MIPS observations. However, de Blok & Walter (2006) find an extended stellar population that exceeds the size of the H I disk (see further discussion in § 1).

tion throughout the disk as well as actively star-forming regions with associated H α emission which were first studied by Hubble (1925). The star formation has been quiescent over the past few Gyr, without major peaks or dips in the absolute rate (Wyder 2001, 2003). de Blok & Walter (2006) derive a total H α flux of $2 \times 10^{39} \text{ erg s}^{-1}$, corresponding to a global H α -based star formation rate (SFR) of $\sim 0.015 M_{\odot} \text{ yr}^{-1}$ using the calibration of Kennicutt (1998).

NGC 6822 boasts an unusual H I distribution; in the extended H I disk (see Figure 1) lies one of the largest known holes in the ISM of a dwarf galaxy, first discussed by de Blok & Walter (2000). de Blok & Walter (2006) argue that this hole is likely caused by the combined effects of stellar evolution. That study also reveals the presence of a significant blue star population in the outer H I disk, and a lower surface brightness, spheroidal red stellar population extending beyond the H I distribution. The extended H I disk may include a dwarf companion galaxy in the northwest region (note that interactions with this system may have played a part in triggering some of the recent star formation in the galaxy; see de Blok & Walter 2000). The well-sampled rotation curve shows that the system is highly dark-matter dominated (Weldrake et al. 2003). The proxim-

ity of NGC 6822 means that it is one of only a few places where the small-scale ($\sim 100 \text{ pc}$) structure of the ISM can be studied at multiple wavelengths.

Previous infrared studies of NGC 6822 have examined the heating and cooling mechanisms in the ISM. Using *InfraRed Astronomical Satellite* (IRAS) data, Gallagher et al. (1991) found a variable H α /FIR ratio within the disk, with roughly 50% of the FIR emission arising from regions that are luminous at H α . The remaining fraction of diffuse IR flux was attributed to a low optical depth (i.e., low dust content) in the ISM. Thus, regions of strong IR emission correspond to comparatively dusty regions that also contain a younger stellar population. A second IRAS study by Israel et al. (1996) found that three of the bright IR peaks were associated with luminous H II regions, while two equally bright sources were unassociated with obvious sources of ionizing radiation. These authors confirm the prominent diffuse dust continuum emission found by Gallagher et al. (1991). Further, they find, using single-temperature blackbody fits to the far-IR data, a dust-to-gas ratio (1.4×10^{-4}) that is much lower than typical values seen in more metal-rich systems such as the Milky Way (average dust-to-gas ratios of ~ 0.006 – 0.01 ; Sodroski et al. [1997], Li [2004]). NGC 6822 was observed with the *In-*

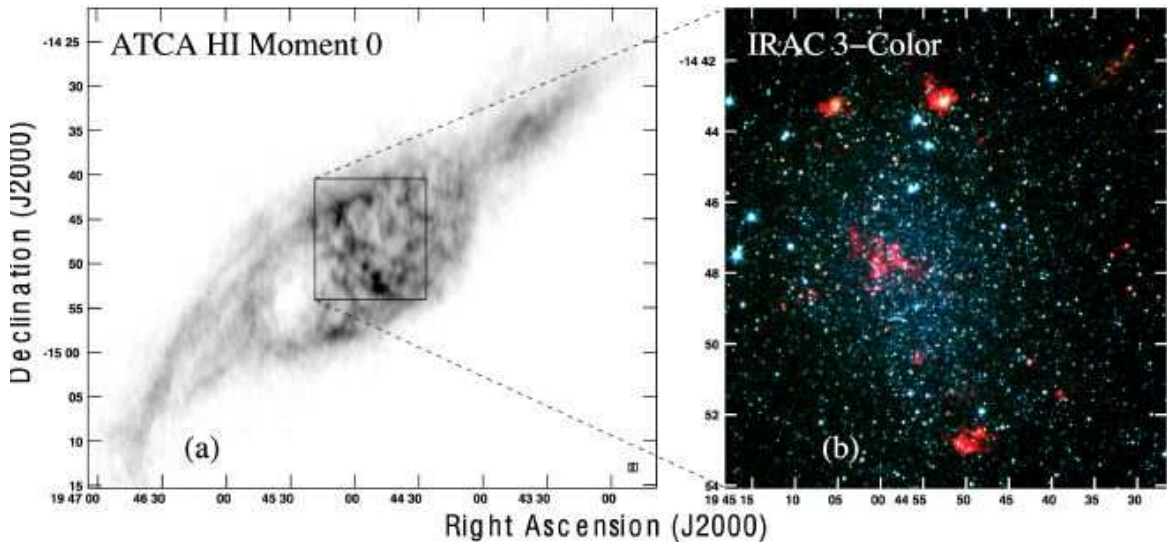


FIG. 2.— H I (a) and IRAC (b) images of NGC 6822. (a) shows the total H I column density distribution (de Blok & Walter 2000), while (b) shows the underlying stellar and warm dust components. The three-color image shows the $3.6 \mu\text{m}$ band as blue, the $4.5 \mu\text{m}$ band as green, and the $8 \mu\text{m}$ band as red; regions of hot dust emission, indicative of active star formation, appear as diffuse regions of red emission. The box in (a) shows the approximate field of view shown in (b).

frared Satellite Observatory at 6.75 and $15 \mu\text{m}$, but only the most luminous H II regions were detected (Dale et al. 2000; Hunter et al. 2001).

In this paper, we present *Spitzer* Infrared Array Camera (IRAC) and Multiband Imaging Photometer for *Spitzer* (MIPS) imaging (see Werner et al. 2004; Fazio et al. 2004; Rieke et al. 2004) of the high optical surface brightness component (i.e., the inner portion of the H I disk) of NGC 6822 (see Figure 2 for a comparison of the field of view imaged and the size of the H I disk). These data were obtained as part of the *Spitzer* Infrared Nearby Galaxies Survey (*SINGS*; see Kennicutt et al. 2003). As the nearest galaxy in the *SINGS* sample, these data probe the nature of mid- and far-IR emission at unprecedented sensitivity and resolution (~ 130 pc; see further discussion below). We compare these *Spitzer* data to sensitive H α , H I and radio continuum imaging in order to study the relation between H I surface density and the locations and intensities of star formation and IR emission.

2. OBSERVATIONS AND DATA REDUCTION

2.1. *Spitzer* Imaging

For an overview of the *SINGS* observational strategies, see Kennicutt et al. (2003). NGC 6822 was observed for 122 minutes in IRAC mosaicing mode on 2004, October 7 and 11; the separate visits to the target ensure proper removal of image artifacts and asteroids. The observations cover the optical extent of the galaxy to the R_{25} level (see Figures 1 and 2). de Blok & Walter (2006) find that the stellar population extends throughout the entire H I distribution; our IRAC data remain insensitive to stars in the outer H I disk of NGC 6822. The *SINGS* IRAC pipeline processes the basic calibrated data (BCD) images, producing mosaics with pixel scales of $0.75''$ and PSF FWHM values of $1.66''$, $1.72''$, $1.88''$, and $1.98''$ at 3.6 , 4.5 , 5.8 and $8 \mu\text{m}$, respectively (Fazio et al. 2004); note that $1'' = 2.4$ pc at the adopted distance of 490 kpc. Flux levels are uncertain at the $\sim 10\%$ level, primarily

due to systematic effects in the calibration process.

MIPS scan mapping mode observations were obtained on 2004, September 24 and 25, for a total of 162.1 minutes. The MIPS Instrument Team Data Analysis Tool (Gordon et al. 2005) was used to process the BCD files, producing mosaic images with pixel scales of $0.75''$, $3.0''$, and $6.0''$ at 24 , 70 and $160 \mu\text{m}$, respectively. Systematic uncertainties (e.g., detector nonlinearities, time-dependent responsivity variations, background removal, etc.) limit the absolute flux calibration to $\sim 10\%$ in the $24 \mu\text{m}$ band and to $\sim 20\%$ in the 70 and $160 \mu\text{m}$ bands (note that the absolute calibration changes slightly depending on which pipeline was used to produce the BCD-level data¹⁴; the S10 calibration is applied to these data). The FWHMs of the PSFs are $6''$, $18''$, and $40''$ at 24 , 70 , and $160 \mu\text{m}$, respectively. All flux densities were extracted from the broadband images after convolution to the $160 \mu\text{m}$ beam. We use convolution kernels that convert an input PSF into a lower resolution output PSF using the ratio of Fourier transforms of the output to input PSFs. High frequency noise in the input PSF is suppressed when these kernels are created. See K. D. Gordon et al. (2006, in preparation) for details.

At the Galactic latitude of NGC 6822 (-14.8°), the foreground stellar contamination is high. The $3.6/8 \mu\text{m}$ and $8/24 \mu\text{m}$ colors were examined in order to remove the brightest foreground sources, which will have the most pronounced effect on derived flux densities. Less luminous sources require a more detailed treatment; a first-order correction can be estimated by computing the strength of foreground star emission in regions that are clearly unassociated with the stellar component of NGC 6822, and scaling these to the sizes of the regions under study (e.g., Lee et al. 2006b). However, the proximity of NGC 6822 makes it large on the sky; the IRAC maps do not include a large overscan region, making this

¹⁴ See the MIPS data analysis handbook for details; <http://ssc.spitzer.caltech.edu/mips>

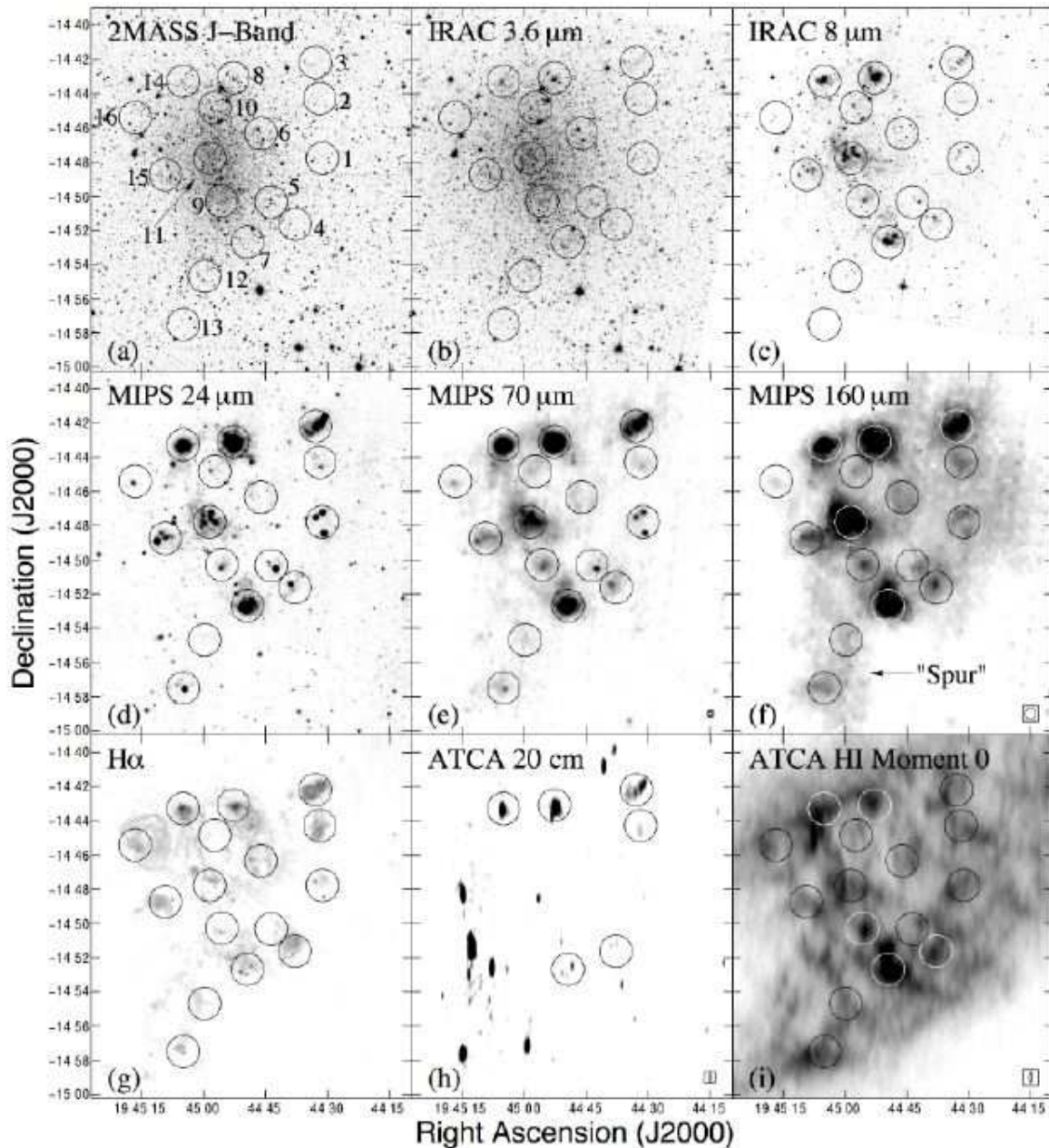


FIG. 3.— 2MASS J (a), 3.6 and 8 μm (b, c), 24, 70, and 160 μm (d, e, f), $\text{H}\alpha$ (g), 20 cm radio continuum (h), and H I spectral line (i) images of NGC 6822. All image scales are linear, except for the $\text{H}\alpha$ image (g), which is shown in a logarithmic stretch to highlight the low-surface brightness ionized gas that permeates much of the central disk of the system. Beam sizes are shown as boxed ellipses for the MIPS and radio data, in the bottom right corners. Overlaid are the sizes and locations of the smaller apertures [diameter = $114'' \simeq 3 \times \text{FWHM}$ ($160 \mu\text{m}$) $\simeq 270 \text{ pc}$] discussed in the text; these regions are labeled in panel (a). Note that the regions that encompass the major IR emission complexes (regions 3, 7, 8, 11, and 14; see also Table 1) have also been analyzed using apertures with four times the area. The 8 μm image does not cover the full field of view shown in panel (c); since the 4.5 μm band has the same orientation, flux densities are not available for region 13 in either of these bandpasses. Note that the radio continuum image in panel (h) shows only the apertures where 20 cm emission is detected; numerous background sources exist within this field of view (see further discussion in § 3.3). The aperture sizes are large enough to cover the bulk of the extended long-wavelength PSFs, minimizing aperture correction effects (see further discussion in § 3).

technique susceptible to small-number statistics. We discuss the effects of foreground contamination in more detail in § 3. Background sources are more difficult to identify (though a first-order estimate of their number density is available from some of the plots shown in this work; see further discussion in § 3.2.1), and no correction for these sources has been explicitly applied.

Foreground Milky Way cirrus contamination is non-negligible in this region of the sky (e.g., Gallagher et al. 1991); given the extent of the galaxy, there will be variations in the cirrus contamination levels within the system that we are unable to remove. In an attempt to subtract the smooth diffuse component, high-surface brightness emission that is clearly associated with the galaxy (by

TABLE 1
INFRARED SOURCES IN NGC 6822

Identification	α (J2000)	δ (J2000)	Previous I.D.	References
NGC 6822-1	19:44:31.28	-14:47:46.69	I96 1	3
NGC 6822-2	19:44:31.92	-14:44:16.70	Hubble II	1
NGC 6822-3	19:44:32.96	-14:42:10.71	Hubble I/III, G91 3, I96 2	1, 2 ^a , 3
NGC 6822-4	19:44:37.89	-14:51:37.79	I96 3	3
NGC 6822-5	19:44:43.69	-14:50:19.86	I96 3	3
NGC 6822-6	19:44:46.18	-14:46:19.89		
NGC 6822-7	19:44:49.47	-14:52:40.93	Hubble IV, G91 1, I96 4	1, 2, 3
NGC 6822-8	19:44:52.81	-14:43:04.97	Hubble V, G91 3, I96 5	1, 2, 3
NGC 6822-9	19:44:55.69	-14:50:17.00		
NGC 6822-10	19:44:57.36	-14:44:50.01		
NGC 6822-11	19:44:58.59	-14:47:47.02	Hubble VI/VII, G91 2, I96 6	1, 2, 3
NGC 6822-12	19:44:59.82	-14:54:41.03		
NGC 6822-13	19:45:04.99	-14:57:29.07	I96 7	3
NGC 6822-14	19:45:05.01	-14:43:17.07	Hubble X, G91 3, I96 8	1, 2, 3
NGC 6822-15	19:45:09.35	-14:48:44.10	Hubble IX, G91 2, I96 9	1, 2, 3
NGC 6822-16	19:45:16.68	-14:45:24.26		

REFERENCES. — 1 - Hubble (1925); 2 - Gallagher et al. (1991); 3 - Israel et al. (1996)

^aThe sources in Gallagher et al. (1991) are not defined by low-resolution ($1.5' \times 5'$) *IRAS* imaging; the cross-identifications here correspond to only the highest-surface brightness IR peaks in the IR or $H\alpha$ images.

comparison with images at multiple wavelengths) was masked, leaving an estimate of the (spatially variable) background cirrus emission. This background information was smoothed by a $6'$ boxcar function and then interpolated over the area of the galaxy. This smoothed cirrus component was then subtracted from the images at 24, 70 and 160 μm . Comparison of flux measurements before and after the cirrus removal shows that this correction is of order $\sim 10\%$. The subtracted components at 70 and 160 μm are in rough agreement (in terms of both morphology and surface brightness) with the lower-resolution COBE/DIRBE maps presented by Schlegel et al. (1998). Given the systematic uncertainties in the long-wavelength bands (see above) and the potential contamination by foreground cirrus emission, and assuming a random error component of up to $\sim 10\%$, these corrections imply a total error budget of $\sim 15\%$ at 24 μm , and $\sim 25\%$ at 70 and 160 μm .

2.2. $H\text{ I}$ Spectral Line and Radio Continuum Imaging

The $H\text{ I}$ moment zero (representing integrated column density) image presented here, first published in de Blok & Walter (2000), was obtained with the *Australia Telescope Compact Array*¹⁵ (*ATCA*) in 1999 and 2000, using the 375, 750D, 1.5A, 6A and 6D configurations. Fifteen 12-hour synthesis observations were taken in mosaicing mode, with the spectral line correlator providing 0.8 km s^{-1} channel separation.

To assure accurate total column density calibration, the interferometric data were combined with single-dish observations taken with the 64-m Parkes telescope. These data use the same channel separation as the interferometric observations. The “zero-spacing” correction was applied in the MIRIAD¹⁶ environment. Conditional

transfer functions (i.e., blanking) were applied to the final cube to create the integrated column density image presented here. The image has a beam size of $42.4'' \times 12''$ ($1\text{ Jy Bm}^{-1} = 1190.5\text{ K}$). The final cube that was imaged to produce the moment zero map has a 5σ column density sensitivity of $1.6 \times 10^{19}\text{ cm}^{-2}$; the peak $H\text{ I}$ column density is $\sim 3 \times 10^{21}\text{ cm}^{-2}$, and the total $H\text{ I}$ mass is $1.34 \times 10^8 M_{\odot}$ at the adopted distance. More detailed discussions of the $H\text{ I}$ data, analysis and interpretation can be found in de Blok & Walter (2000), Weldrake et al. (2003), and de Blok & Walter (2006).

During the acquisition of the *ATCA* $H\text{ I}$ data, a second frequency band was simultaneously observed; centered at 1.38 GHz, this 128 MHz bandwidth channel provides a sensitive L-band radio continuum map of NGC 6822. Note that these data have no zero-spacing correction applied; the presence of comparatively strong background sources and the weak nature of the intrinsic radio continuum in NGC 6822 make integrated total flux densities difficult to determine. Single-dish observations at other frequencies (Klein et al. 1983; Klein & Gräve 1986) suggest an integrated L-band flux density of $100 \pm 25\text{ mJy}$ (Israel et al. 1996). Comparing with our interferometric flux density measurements (see § 3 below) suggests that the high surface brightness radio components account for $\sim 70\%$ of the (uncertain) total L-band flux density. The remainder may exist as a diffuse synchrotron component (see more detailed discussion on the thermal/nonthermal decomposition within the galaxy in § 3.3). The radio continuum data use the same basic reductions as for the spectral line data, though the final image has a smaller beam size of $30'' \times 8''$; the rms noise is $\sim 90\text{ }\mu\text{Jy Bm}^{-1}$. Note that the 20 cm image presented in Figure 3(h) shows only the apertures with radio detections. Further, there are numerous background radio sources in the field (see also the discussion in § 3.3).

¹⁵ The Australia Telescope is funded by the Commonwealth of Australia for operation as a National Facility managed by the Commonwealth Scientific and Industrial Research Organisation.

¹⁶ See <http://www.atnf.csiro.au/computing/software/miriad>

2.3. Deep $H\alpha$ Imaging

TABLE 2
OBSERVED QUANTITIES IN NGC 6822^a

Region ^b	H α (erg s ⁻¹ cm ⁻²)	3.6 μ m ^c (mJy)	4.5 μ m ^c (mJy)	5.8 μ m ^c (mJy)	8.0 μ m ^c (mJy)	24 μ m (mJy)	70 μ m (mJy)	160 μ m (mJy)	20 cm (mJy)	H I (Jy km s ⁻¹)
Aperture radii = 57'' = 3 \times (160 μ m PSF FWHM \gtrsim 130 pc)										
1	(9.6 \pm 1.9)E-13	24 \pm 3	16 \pm 2	16 \pm 2	28 \pm 4	100 \pm 16	560 \pm 140	2100 \pm 530	\lesssim 1.0 \pm 0.3	12.9 \pm 1.3
2	(26 \pm 5)E-13	17 \pm 2	12 \pm 2	6 \pm 0.6	15 \pm 2	20 \pm 3	470 \pm 120	2100 \pm 530	3.3 \pm 0.4	12.2 \pm 1.2
3	(110 \pm 20)E-13	17 \pm 2	14 \pm 2	11 \pm 2	27 \pm 4	110 \pm 17	1700 \pm 430	3700 \pm 930	12 \pm 1.2	12.0 \pm 1.2
4	(24 \pm 5)E-13	31 \pm 4	21 \pm 3	20 \pm 3	26 \pm 3	32 \pm 5	630 \pm 160	2100 \pm 530	3.1 \pm 0.4	14.8 \pm 1.5
5	(5.0 \pm 1)E-13	43 \pm 5	29 \pm 3	26 \pm 3	27 \pm 3	81 \pm 13	600 \pm 150	1600 \pm 400	\lesssim 1.0 \pm 0.3	11.0 \pm 1.1
6	(14 \pm 3)E-13	55 \pm 6	38 \pm 4	34 \pm 4	33 \pm 4	17 \pm 3	520 \pm 130	2000 \pm 500	\lesssim 1.0 \pm 0.3	10.1 \pm 1.0
7	(24 \pm 5)E-13	42 \pm 5	29 \pm 3	49 \pm 6	84 \pm 10	260 \pm 40	2300 \pm 580	4900 \pm 1300	6.4 \pm 0.7	21.8 \pm 2.2
8	(120 \pm 25)E-13	49 \pm 6	39 \pm 4	65 \pm 8	130 \pm 14	780 \pm 120	4300 \pm 1100	6800 \pm 1700	21 \pm 2.1	14.0 \pm 1.4
9	(4.6 \pm 0.9)E-13	74 \pm 8	49 \pm 4	47 \pm 5	41 \pm 4	23 \pm 4	900 \pm 230	2100 \pm 530	\lesssim 1.0 \pm 0.3	13.7 \pm 1.4
10	(4.8 \pm 1.0)E-13	62 \pm 7	43 \pm 4	44 \pm 5	41 \pm 5	31 \pm 5	900 \pm 230	1700 \pm 430	\lesssim 1.0 \pm 0.3	9.1 \pm 0.9
11	(13 \pm 3)E-13	92 \pm 10	60 \pm 7	76 \pm 9	100 \pm 12	97 \pm 15	2000 \pm 500	5200 \pm 1300	\lesssim 1.0 \pm 0.3	15.1 \pm 1.5
12	(5.9 \pm 1.2)E-13	30 \pm 3	22 \pm 3	18 \pm 2	11 \pm 2	8.7 \pm 1.3	380 \pm 100	1400 \pm 350	\lesssim 1.0 \pm 0.3	11.0 \pm 1.1
13	(6.8 \pm 1.4)E-13	12 \pm 2	N/A	10 \pm 1	N/A	30 \pm 5	480 \pm 120	1700 \pm 430	\lesssim 1.0 \pm 0.3	14.1 \pm 1.4
14	(110 \pm 20)E-13	35 \pm 4	28 \pm 3	32 \pm 4	49 \pm 6	190 \pm 29	2400 \pm 600	3800 \pm 950	11 \pm 1.1	16.3 \pm 1.6
15	(17 \pm 4)E-13	54 \pm 6	39 \pm 4	41 \pm 5	39 \pm 4	75 \pm 12	880 \pm 220	2100 \pm 530	\lesssim 1.0 \pm 0.3	10.6 \pm 1.1
16 ^d	(17 \pm 4)E-13	26 \pm 3	20 \pm 2	16 \pm 2	10 \pm 6	9.4 \pm 1.4	330 \pm 85	610 \pm 160	\lesssim 1.0 \pm 0.3	11.6 \pm 1.2
Aperture radii = 114'' = 6 \times (160 μ m PSF FWHM) \gtrsim 260 pc										
Total Galaxy ^e										
Total	(700 \pm 140)E-13	2.26 \pm 0.23	1.44 \pm 0.15	1.90 \pm 0.19	1.87 \pm 0.19	2.51 \pm 0.50	53.2 \pm 15	136.2 \pm 40.0	69.4 \pm 14 ^f	2266 \pm 227

^aAll values derived without aperture corrections (see discussion in § 2 and § 3); the 24, 70 and 160 μ m images have had a first-order estimate of the Galactic cirrus component removed. The IRAC flux densities may have sizeable aperture corrections (especially in the 5.8 and 8.0 μ m bands, where the corrections will be of order \sim 10% for the 57'' radius apertures, and as large as \sim 25% for the global flux density).

^bSee Table 1 for source coordinates and cross-identifications.

^cOnly the brightest foreground sources have been removed in deriving these values. Using a limited number of apertures which sample regions clearly unassociated with NGC 6822, we derive the following potential contamination levels from unsubtracted foreground sources: IRAC 3.6 μ m = 11.2 \pm 4.2 mJy; IRAC 4.5 μ m = 12.0 \pm 5.1 mJy; IRAC 5.8, 8.0 μ m have average foreground values consistent with zero).

^dUncertain local background value in the IR.

^eSpitzer global flux densities listed in units of Jy.

^fCalculated as the sum of individual sources, using the larger aperture when available.

The H α image presented here was obtained with the 2.5m Isaac Newton Telescope, using three pointings with the Wide Field Camera to cover the entire H I disk of NGC 6822. The integration time was 80 minutes per pointing; wide-filter R-band imaging was used to remove the continuum. Flux calibration was obtained by comparison with published fluxes for high-surface brightness regions in Hodge et al. (1988, 1989), after correction for foreground reddening (E(B-V) = 0.24; Gallart et al. 1996a). The limiting flux level is \sim 3.7 \times 10⁻¹⁸ erg s⁻¹ cm⁻², roughly a factor of ten deeper than the images presented by Hodge and collaborators. For a detailed discussion of the H α image handling, see de Blok & Walter (2006).

3. MULTIWAVELENGTH EMISSION IN NGC 6822

Multiwavelength imaging of NGC 6822 reveals a wealth of detail and structure in the stellar and gaseous components. In Figure 3 we present images of the central region of the galaxy at nine different wavelengths. In the 2MASS J (Jarrett et al. 2003) and 3.6 μ m bands [see Figures 3(a) and 3(b)], the red stellar component of the galaxy is smoothly distributed, with few major stellar concentrations or clusters (compare to Wyder 2001, 2003 and de Blok & Walter 2006 for more detailed views of the system at optical wavelengths). Longward of 4 μ m, the spectral energy distribution (SED) of the stellar population has dropped off sufficiently that the warm dust emission from active star formation regions dominates the galaxy morphology (see the 8 μ m image in Figure 3(c).

Moving into the FIR, Figures 3d, e, and f show that the active regions of star formation stimulate warm dust emission throughout the system. There is also very cool dust extending to the south of the major star formation regions (though still well within the optical and H I radii; see Figure 3f); comparing this emission with the H α and H I images shown in Figures 3(g) and 3(i) leaves little doubt that it is associated with NGC 6822 and is not an image artifact. Indeed, both Gallagher et al. (1991) and Israel et al. (1996) recover this structure in *IRAS* maps. Further, de Blok & Walter (2003) find that this region (spatially coincident with the rim of the H I hole) has the largest concentration of blue stars in NGC 6822.

The H α image presented in Figure 3(g) shows that there is ionized gas throughout much of the central disk of the galaxy; previous observations and comparisons with IR imaging have concentrated on the higher-surface brightness star formation regions (e.g., Gallagher et al. 1991; Israel et al. 1996). Six of these regions correspond to detections in the ATCA radio continuum image shown in Figure 3(h). Note that there are numerous background sources in the radio continuum field of view; we have classified radio “detections” as areas of $> 5\sigma$ flux density, that have spatial counterparts in H α and the 24, 70 and 160 μ m bands (note that we only show the apertures with radio detections in Figure 3h). Finally, the H I distribution (Figure 3i) throughout the central region of the galaxy contains mostly high-surface brightness (i.e., H I columns \gtrsim 10²¹ cm⁻²) emission. There is clumping of the neutral gas surrounding various emission peaks in

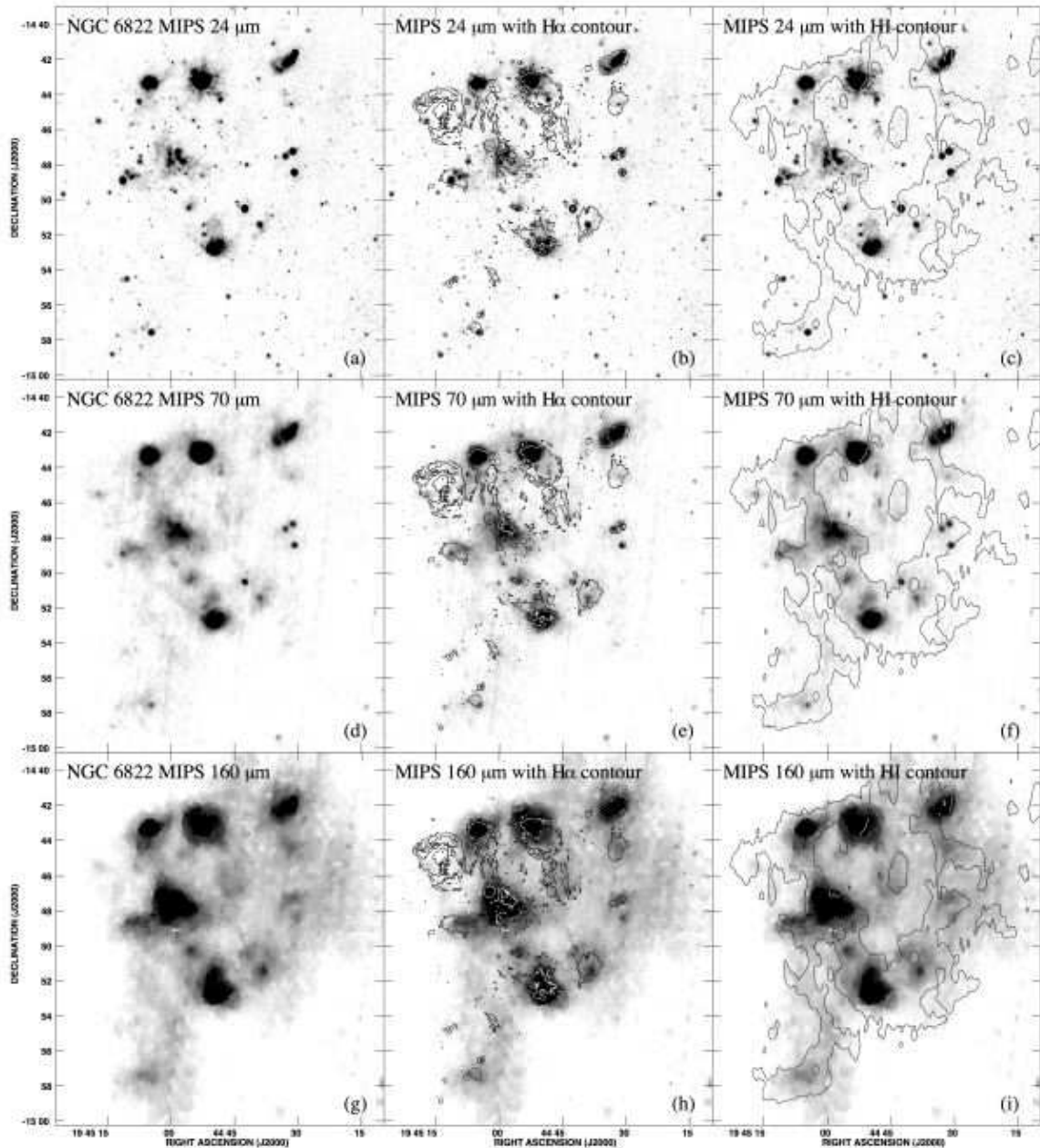


FIG. 4.— The 24 (a, b, c), 70 (d, e, f) and 160 μm images (g, h, i) of NGC 6822, with H α (b, e, h) and H I (c, f, i) contours overlaid. The H α contour is at the flux level of $3.8 \times 10^{-18} \text{ erg s}^{-1} \text{ cm}^{-2}$, highlighting low-level nebular emission throughout the disk; the H I contour is at the level of 10^{21} cm^{-2} , highlighting the canonical surface density threshold for star formation. Note the striking correspondence between nebular, dust continuum, and H I emission.

other wavebands.

We study the panchromatic emission from 16 regions throughout the galaxy; these regions are shown as circles overlaid on the various panels of Figure 3, and their positions and cross-identifications are given in Table 1. The aperture locations were chosen primarily to probe the IR emission complexes. The aperture sizes and locations represent a compromise between spatial resolution, minimization of aperture effects, and diversity of regions that can be probed. The aperture diameter of $114''$ ($= 270 \text{ pc}$ at the adopted distance) is $\sim 3 \times$ larger than the FWHM of the 160 μm PSF (and considerably larger than the FWHM of the 70 μm , 24 μm , and IRAC

bands), which should alleviate serious aperture corrections to the measured flux densities (especially at 3.6, 4.5, 24 and 70 μm ; extended-source aperture corrections at 5.8 and 8.0 are still uncertain, but may be as large as $\sim 30\%$). For example, an aperture-centered point source at 160 μm would have an aperture correction of $\sim 30\%$; this factor will be smaller for extended emission which fills the beam (as is the case for most of the 160 μm sources in the galaxy; however, the size of the correction will depend on the IR surface brightness in the regions surrounding the apertures as well). This chosen aperture size is well-matched to most of the discrete dust emission regions in the galaxy, while still allowing us to

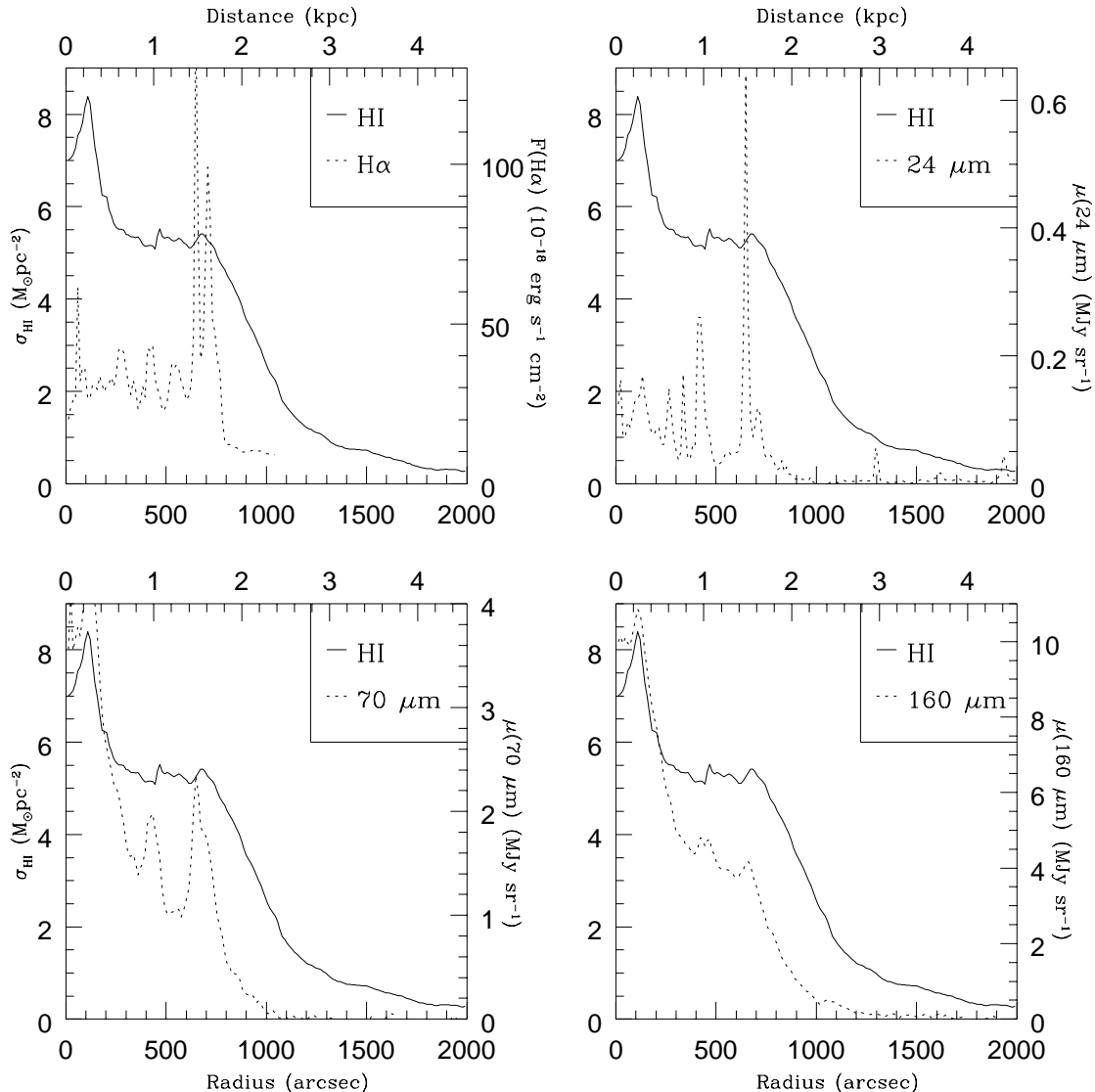


FIG. 5.— Surface brightness profiles of H I emission, overlaid with profiles of H α emission (a), and 24, 70 and 160 μm emission (b, c, d). The solid line and left-hand y-axis label in each panel correspond to the H I surface density in units of $M_{\odot} \text{pc}^{-2}$ (not inclination corrected); the dotted lines and right-hand y-axis labels correspond to the flux levels in H α (in units of $\text{erg sec}^{-1} \text{cm}^{-2}$) or to IR surface brightness values (in units of MJy sr^{-1}). These profiles were created using the same parameters as the rotation curve analysis of Weldrake et al. (2003); the central location is $(\alpha, \delta) = 19:44:58.04, -14:49:18.9$ (J2000; this location is between apertures 9 and 11 in Figure 3), and an average position angle $\simeq 120^{\circ}$ is used. The profiles integrate across the high-S/N ($\geq 3\sigma$) regions of the images shown in Figures 3 and 4.

resolve variations in the nature of the FIR emission by using a large number of apertures. Table 2 shows the flux densities derived in each aperture from H α to the radio regime. Note the footnotes to that table, which quantify the effects of foreground stellar contamination in the short-wavelength data. We also investigate the effects of expanding the apertures by a factor of 4 in area for the five brightest dust emission complexes (see further discussion in § 3.1). Table 3 presents various quantities derived from the measurements. We derive an estimate of the 3-1000 μm total infrared flux (TIR) using equation 4 of Dale & Helou (2002), evaluated at the effective MIPS wavelengths:

$$TIR = (10^{-14})(19.74 \cdot S_{24} + 3.23 \cdot S_{70} + 2.59 \cdot S_{160}) \quad (1)$$

where S_{24} , S_{70} and S_{160} are the measured flux densities

in units of Jy. Table 3 also presents the H α /TIR ratio, the dust-to-gas ratio (see more detailed discussion below, and also Tables 3 and 4), and the ratio of TIR/radio luminosity as represented by the radio-FIR correlation coefficient “q”; each of these quantities will be discussed in more detail below.

3.1. Linking Heating Sources with the Dust Continuum

3.1.1. H α vs. IR Emission

The major H II regions Hubble I/III, V, and X (regions 3, 8, and 14 in Figure 3, respectively) are the strongest H α sources in the galaxy. These regions are also luminous at 24, 70 and 160 μm . However, the relative strengths of H α and TIR emission vary considerably from one source to the next; the regions of strongest H α

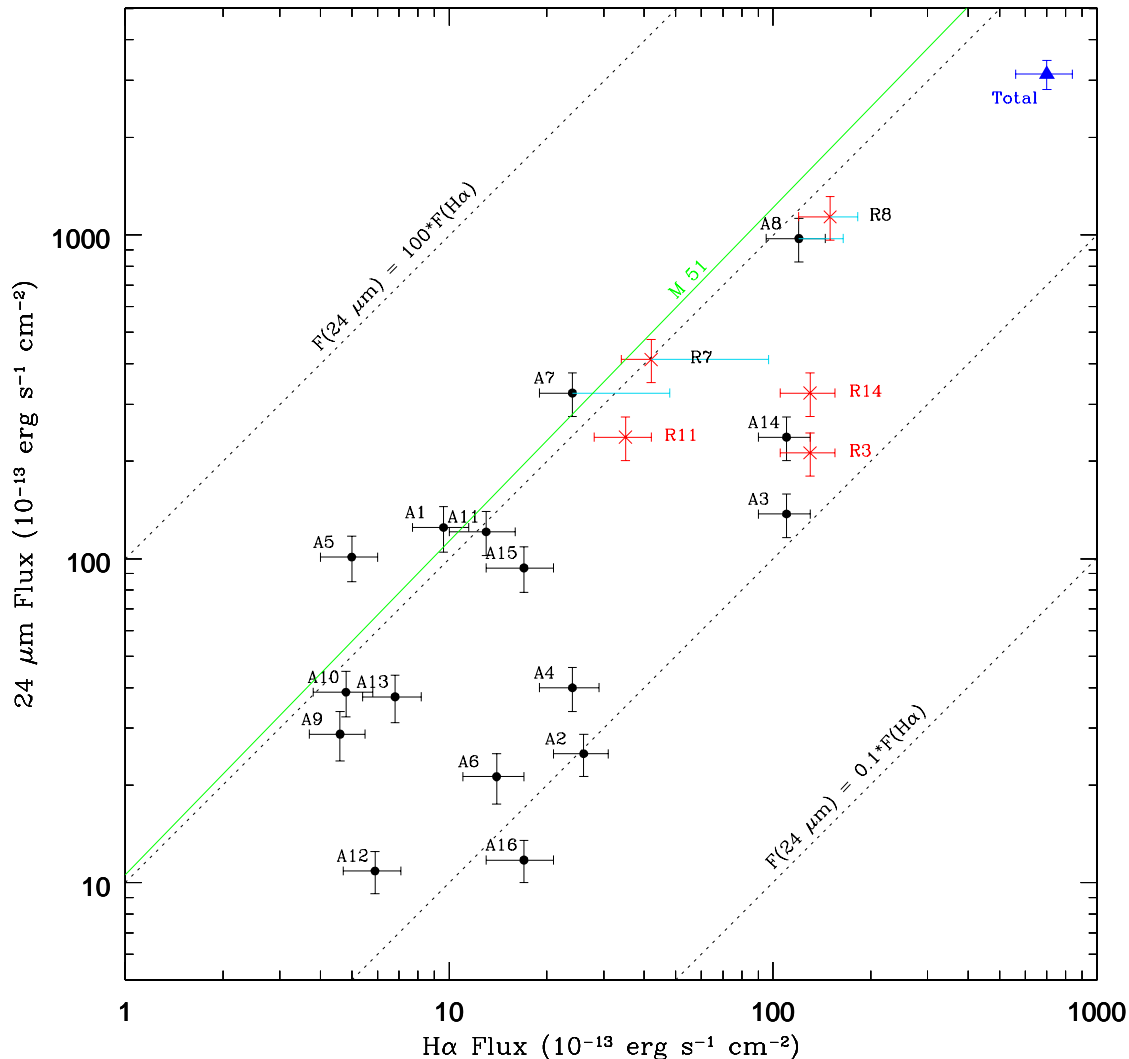


FIG. 6.— Comparison of measured fluxes at $H\alpha$ and $24\ \mu\text{m}$; black points indicate the 16 regions shown in Figure 3; red points show the five larger apertures used for the major IR peaks (see Table 2); the blue point shows photometry for the entire galaxy. Asymmetric errorbars on points for regions 7 and 8 (shown in cyan) demonstrate the magnitude of the measured extinctions at $H\alpha$, as inferred from comparing (thermal) radio continuum and $H\alpha$ emission strengths (see discussion in § 3.1.1). The $24\ \mu\text{m}$ flux is calculated using the techniques discussed in Calzetti et al. (2005), where $F_{24} = S_{24} \times \nu_{24}$; values of S_{24} (in Jy) are taken from Table 2, and the frequency is evaluated at the wavelength of $24\ \mu\text{m}$. The relation derived by Calzetti et al. (2005) for optically thick H II regions in M 51 is shown by the solid green line. The dotted lines show relations of direct proportionality, as labeled, for reference.

and TIR emission are not always co-spatial. There are 5 sources in the galaxy with TIR fluxes ≥ 1.5 Jy (regions 3, 7, 8, 11, and 14; see Table 3); amongst these regions, the $H\alpha$ /TIR ratio varies by a factor of ten, with region 11 having strong TIR emission but weak $H\alpha$, and with region 3 having strong $H\alpha$ compared to TIR. Expanding these apertures by a factor of 2 in radius shows the same trends, but with reduced extrema (a factor of 5 variation in the $H\alpha$ /TIR ratio is found between regions 11 and 3). Similar scatter is seen across the entire sample of 16 regions (see Table 2).

We now examine what fraction of the observed variations can be attributed to extinction effects. Recent work by Wyder (2003) and Lee et al. (2006a) shows that there is variable extinction throughout the disk, with

some regions showing no optical extinction and others showing A_V values up to ~ 2 magnitudes. For strongly star-forming regions with low $H\alpha$ /TIR ratios (e.g., regions 7 and 11), the $H\alpha$ flux (and, correspondingly, the $H\alpha$ /TIR ratio) may be up to 6 times larger than observed after correction for potentially strong internal extinction (Lee et al. 2006a). It should be noted, however, that these values were extracted using $1.5''$ -wide spectroscopic slits, and thus probe extinction on a much smaller spatial scale than we are sensitive to with our *Spitzer* data. Thus, while extinction can play a localized role in some regions, it cannot account entirely for the observed variation in the $H\alpha$ /TIR ratio.

A second measure of the extinction is available by comparing $H\alpha$ and radio continuum emission strengths. For

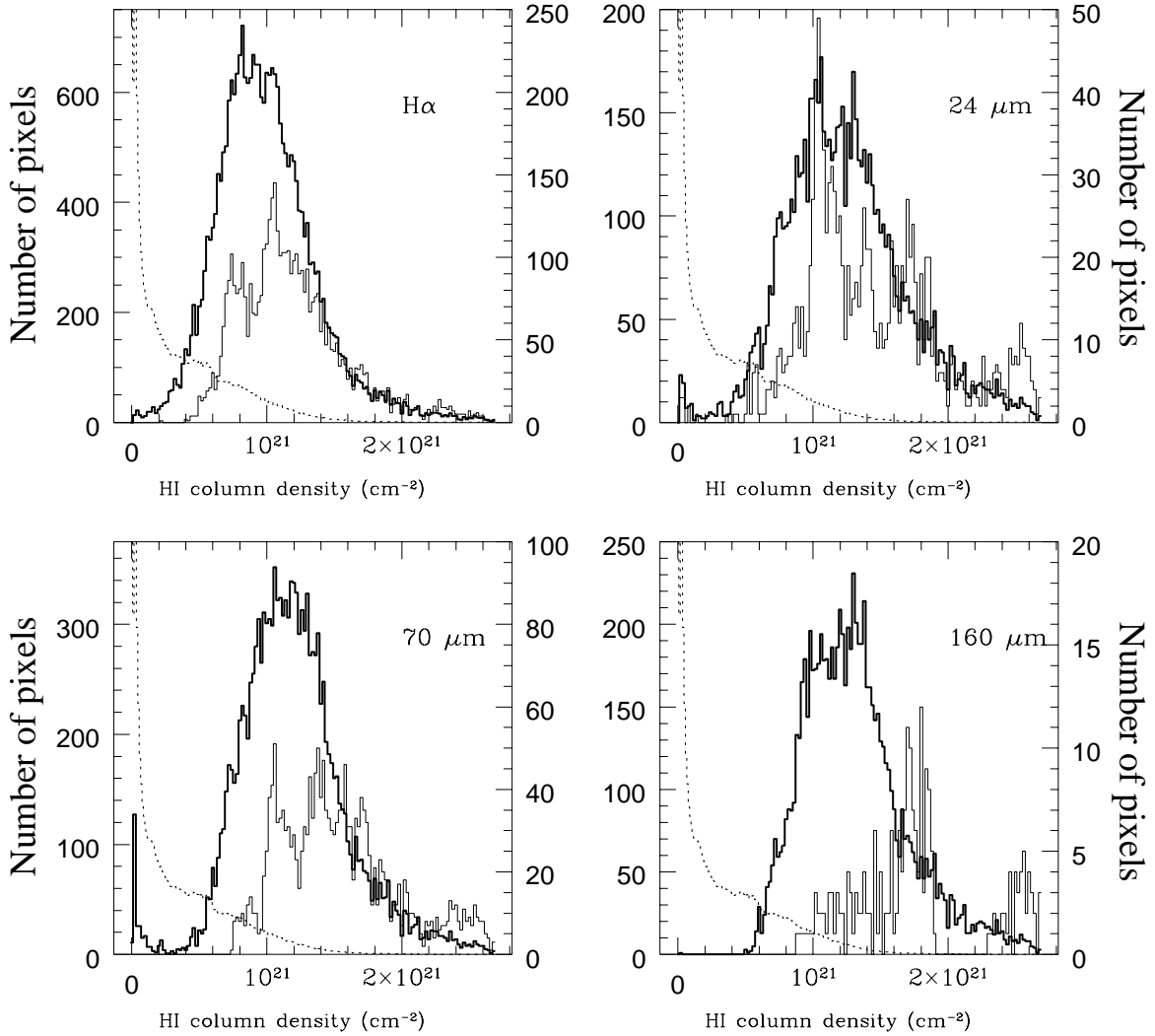


FIG. 7.— Histograms of H I column densities where high-surface brightness H α and FIR emission are detected. The thick black lines correspond to flux levels of $\sim 3.7 \times 10^{-18} \text{ erg s}^{-1} \text{ cm}^{-2}$ (H α) or to surface brightness levels of 4 MJy sr^{-1} (IR), and are enumerated by the left-hand y-axis of each plot; the thin gray lines correspond to flux levels of $\sim 1.4 \times 10^{-17} \text{ erg s}^{-1} \text{ cm}^{-2}$ (H α) or to surface brightness levels of 16 MJy sr^{-1} (IR), and are enumerated by the right-hand y-axis of each plot. The dotted line shows the histogram of H I column densities throughout the entire galaxy, normalized arbitrarily. These plots demonstrate that nebular and dust emission are strongly correlated with regions that are rich in H I gas.

this comparison, we assume that the 20 cm flux densities shown in Table 2 arise from thermal emission processes. This assumption is justified for most of the major H II regions in the galaxy, based on two lines of evidence. First, multi-frequency radio continuum data using both interferometric (Condon 1987) and single-dish (Klein et al. 1983; Klein & Gräeve 1986) observations as compiled in Israel et al. (1996) show that NGC 6822 is extraordinarily weak in the nonthermal radio continuum – nearly all of the emission throughout the galaxy appears to be of a thermal origin. Second, applying the relations in Caplan & Deharveng (1986), and assuming the T_e values calculated in Lee et al. (2006a), we can use our observed (i.e., not extinction-corrected) H α fluxes to predict lower limits for the strengths of thermal radio continuum emission. This exercise shows that nearly all regions have a small or (in most cases) negligible non-thermal component: only regions 7 (Hubble IV) and 8 (Hubble V) show thermal fractions less than 90% ($\sim 50\%$

and 70% in regions 7 and 8, respectively). This suggests that these two regions, both active in current star formation (as evidenced by their strong H α and IR emission), have produced sufficient numbers of SNe to accelerate the relativistic electrons that give rise to the apparent nonthermal components.

We now calculate inferred reddening values, proceeding with the assumption that thermal emission dominates throughout the galaxy. Of the six regions detected in the radio continuum, only regions 7 and 8 show potentially strong inferred reddening values ($A_{\text{H}\alpha} \gtrsim 0.25$ magnitudes). Regions 2, 3, 4, and 14 are consistent with values of $A_{\text{H}\alpha} < 0.1$ magnitude. Note that if regions 7 and 8 do in fact contain a (relatively) strong synchrotron component, then the (smaller) thermal fraction of the detected flux densities puts a yet stronger constraint on the low inferred values of the reddening. The smaller inferred extinctions using this approach compared to the values derived from long-slit spectroscopy (Lee et al. 2006a) are

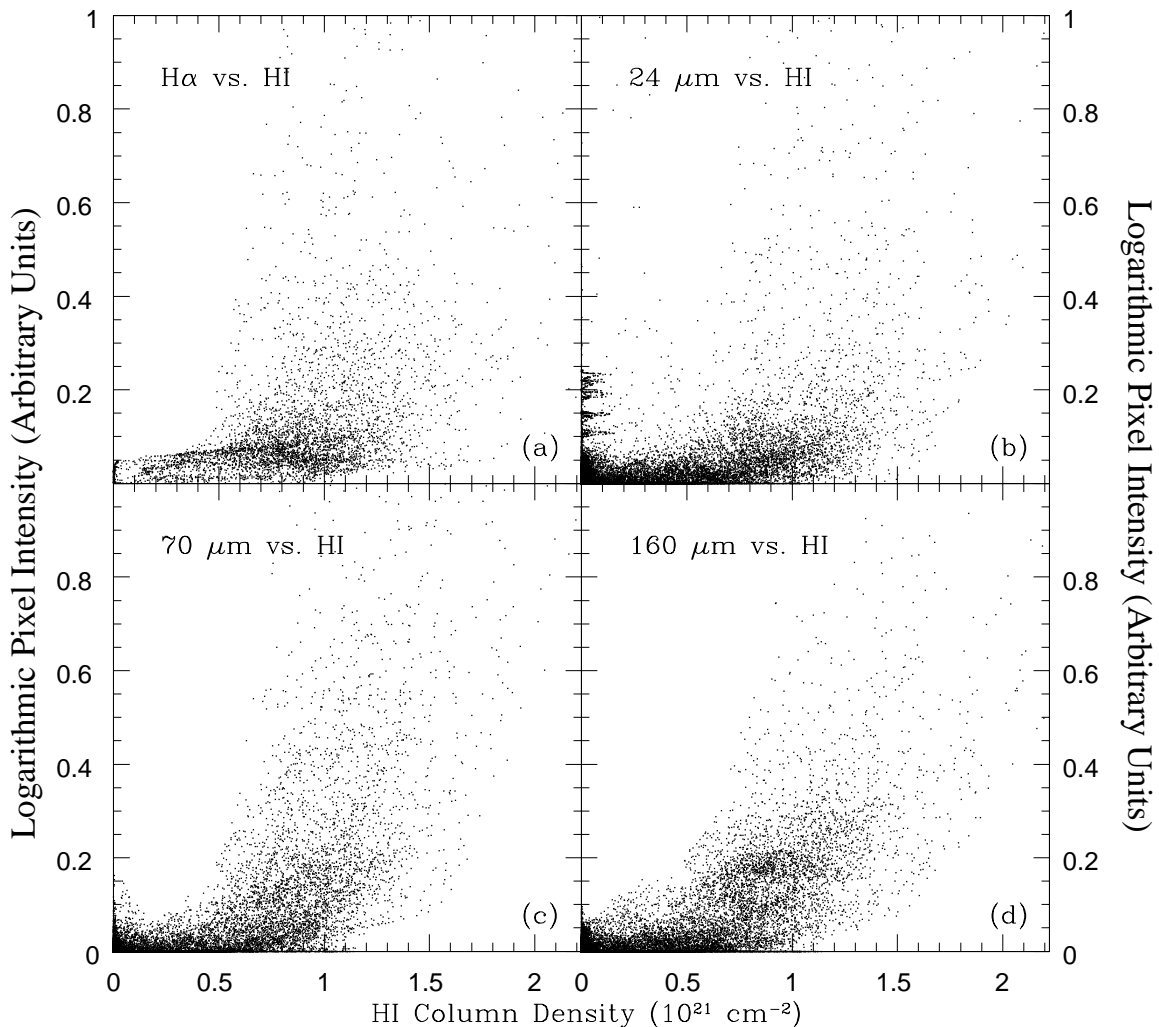


FIG. 8.— Pixel-by-pixel comparison of the strengths of H I and H α (a), 24 μm (b), 70 μm (c), and 160 μm (d) emission. From these plots it is clear that both nebular and dust emission is found preferentially in regions of high H I column density. The 24 and 70 μm plots (b, c) are contaminated by foreground stars and background galaxies at low column densities; a first-order estimate of the severity of the contamination is available by comparing these panels.

expected, since the latter data probe smaller-scale dust concentrations.

To investigate the localized effects of photon absorption and re-radiation in the IR, the central column of Figure 4 presents detailed comparisons of the H α and IR morphologies. Here, a low-level H α flux contour ($3.7 \times 10^{-18} \text{ erg s}^{-1} \text{ cm}^{-2}$) is overlaid on each of the 24, 70 and 160 μm images. It is immediately clear that the regions of high H α and IR surface brightnesses are directly linked, since the H α contours surround the IR emission peaks. We are thus observing localized dust heating in the ISM (see also further discussion below). However, it is also interesting to note that a significant fraction of the integrated IR flux density of the galaxy is unassociated with regions that are luminous at H α . Most H α -bright regions are also luminous in the IR; one notable exception is region 16 (see Figure 3), which shows (low-level) H α emission in a clear shell morphology but

which lacks strong associated dust emission. However, we treat region 16 with caution, since the local background is not well-defined (see Table 2) and may be over-subtracted in the IR images.

To discern the origin of the photons that give rise to IR emission throughout the galaxy, it is useful to quantify what fraction of the total IR luminosity of NGC 6822 arises from regions that are not luminous at H α . The global flux densities in the long-wavelength bands, measured over the entire central disk region ($S_{24} = 2.51 \pm 0.50 \text{ Jy}$; $S_{70} = 53.2 \pm 15 \text{ Jy}$; $S_{160} = 136.2 \pm 40 \text{ Jy}$; see Figure 3 and Table 2), appear to consist of discrete FIR peaks and a more extended “diffuse” component. Here we classify emission as diffuse if it is located outside the regions detected at H α (shown as the $3.7 \times 10^{-18} \text{ erg s}^{-1} \text{ cm}^{-2}$ contour in Figure 4). The quantification of the fraction of the total FIR that arises in a diffuse component is dependent on the sensitivity

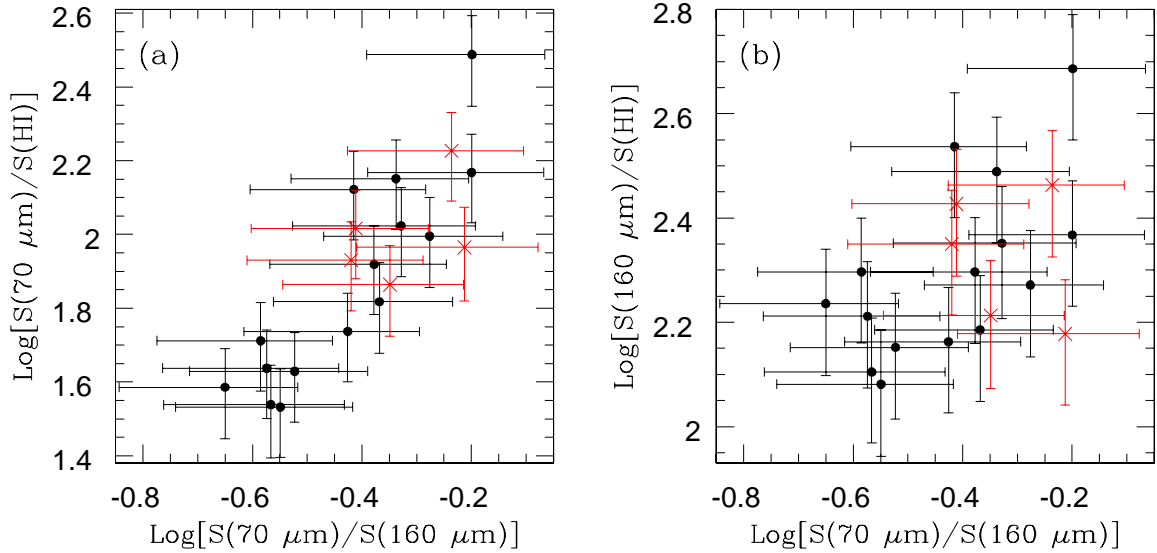


FIG. 9.— Ratios of IR to H I emission strength as a function of dust temperature: (a) shows that as the dust temperature increases (i.e., higher radiation field strengths), there is more 70 μm emission per unit H I mass; this suggests that local star formation is an important parameter in determining the characteristics of IR emission. (b) shows that cooler dust is less sensitive to heating; while a marginal trend exists for higher 160 μm fluxes per unit H I mass in higher-temperature environments, it is less evident than at 70 μm (as expected). Small-radius (57'') apertures are shown as black points, while larger-radius apertures (114'') are shown in red. Note that region 16 is not plotted, since the local background is not well-defined.

of the H α data to which we compare the IR images (or, equivalently, on the surface brightness below which we classify IR emission as “diffuse”). The spatial scales over which the diffuse emission are found are much larger than the PSFs at 160 and (especially) 70 μm (precluding PSF smearing as the only origin of the diffuse component). We find that $> 60\%$ of the integrated flux densities at 70 and 160 μm arise from this diffuse component. While the 24 μm emission is more strongly peaked in regions of active star formation (e.g., Helou et al. 2004; Calzetti et al. 2005), the diffuse component still accounts for $\sim 50\%$ of the total 24 μm flux density. These results suggest that a substantial amount of the IR radiation may be powered by non-ionizing sources or may be the result of UV photons escaping directly from star formation regions; this is discussed further in § 4. Similar results were obtained for NGC 6822 by Gallagher et al. (1991) and Israel et al. (1996); diffuse far-IR emission is also seen in other nearby dwarf galaxies (e.g., NGC 55; Engelbracht et al. 2004).

In Figure 5 we present elliptical surface brightness profiles of H I, H α and IR emission. These profiles were derived using parameters from the H I rotation curve analysis of de Blok & Walter (2000) and Weldrake et al. (2003). Radially-averaged elliptical annuli with 12'' thickness are integrated along the position angle of the galaxy’s major axis [central position: $\alpha = 19:44:58.04$, $\delta = -14:49:18.9$ (J2000; this location is between apertures 9 and 11 in Figure 3); position angle $\simeq 120^\circ$; see Weldrake et al. 2003 for details]. The resulting surface brightness profiles show that H α , IR and H I peaks correlate remarkably well. In particular, the H α and 24 μm profiles are very similar, tracing the local star formation rate (Helou et al. 2004; Calzetti et al. 2005). We discuss the surface brightness profiles in more detail in § 3.2.

3.1.2. Infrared vs. Optical Luminosities and Star Formation Rates

The metal-poor ISM of NGC 6822 is an interesting environment in which to compare the luminosities and implied SFRs from various methods. Using the global flux densities in the long-wavelength bands (see above) and the relations presented in Dale & Helou (2002), the total IR flux of $\sim 5.7 \times 10^{-12} \text{ W m}^{-2}$ corresponds to $L_{\text{TIR}} \simeq 1.6 \times 10^{41} \text{ erg s}^{-1}$ at 490 kpc. The H α -based SFR (sensitive to recent star formation over the last ~ 10 Myr) is $\sim 0.016 M_\odot \text{ yr}^{-1}$, and the total recent SFR (over the last ~ 100 -200 Myr) derived from the stellar population study of Gallart et al. (1996b) is $\sim 0.04 M_\odot \text{ yr}^{-1}$.

The 24 μm luminosity (L_{24}), which has been shown to correlate well with regions of active star formation in a range of environments (e.g., Helou et al. 2004; Calzetti et al. 2005), is an appropriate IR-based SFR indicator for dust-rich regions. We compare the $L_{24}/\text{H}\alpha$ ratio for NGC 6822 with what was observed by Calzetti et al. (2005) in the more metal-rich spiral galaxy M 51 (Bresolin et al. 2004), as follows:

$$\text{Log}(L_{24}) = 1.03 \text{Log}(L_{\text{H}\alpha}) - 0.06945 \quad (2)$$

where L_{24} and $L_{\text{H}\alpha}$ are the observed luminosities at 24 μm and H α , respectively; the intrinsic H $\alpha/P\alpha$ ratio is assumed to be 8.734. The central wavelength of 24.0 μm is used to convert the 24 μm flux density to a luminosity measurement [thus, L_{24} as defined above is not strictly a luminosity, but is rather equivalent to $\nu \cdot F_\nu$; we keep the above notation to allow direct comparison to the work of Calzetti et al. (2005)]. Using the total observed H α luminosity of the system (see Table 2), this relation predicts a total 24 μm luminosity ~ 3 times higher than the observed value. This confirms that metal-poor galaxies do not have enough metals to form dust in the same fraction as more metal-rich environments.

To explore the relation between H α and IR emission on a spatially resolved basis, we plot in Figure 6 the H α vs. 24 μm fluxes, and compare to the relation de-

TABLE 3
DERIVED PROPERTIES OF NGC 6822

Region ^a	S(TIR) ^b (10^{-13} W m ²)	F(H α)/F(TIR) ^c	H I Mass (10^5 M $_{\odot}$)	M _{Dust} /M _{H I} ^d (\mathcal{D})	q _{TIR} ^e	q ₇₀ ^e	q ₂₄ ^e
Aperture radii = 57'' \simeq 3 \times (160 μ m PSF FWHM \simeq 130 pc)							
1	1.03 \pm 0.41	9.6 \pm 4.3	7.3 \pm 0.8	0.0038 \pm 0.0021
2	0.73 \pm 0.29	36 \pm 16	6.9 \pm 0.7	0.0045 \pm 0.0024	2.76	2.15	0.78
3	1.98 \pm 0.79	55 \pm 24	6.8 \pm 0.7	0.0048 \pm 0.0026	2.66	2.15	0.96
4	0.85 \pm 0.34	28 \pm 13	8.4 \pm 0.9	0.0039 \pm 0.0021	2.87	2.31	1.01
5	0.80 \pm 0.32	6.3 \pm 2.8	6.2 \pm 0.7	0.0034 \pm 0.0018
6	0.76 \pm 0.30	18 \pm 8	5.7 \pm 0.7	0.0046 \pm 0.0025
7	2.88 \pm 1.15	8.3 \pm 3.8	12.4 \pm 1.2	0.0037 \pm 0.0020	3.08	2.56	1.61
8	5.39 \pm 2.16	23 \pm 10	7.9 \pm 0.8	0.0073 \pm 0.0039	2.83	2.31	1.57
9	0.91 \pm 0.36	5.1 \pm 2.2	7.8 \pm 0.8	0.0026 \pm 0.0014
10	0.69 \pm 0.28	7.0 \pm 3.2	5.2 \pm 0.6	0.0020 \pm 0.0010
11	2.40 \pm 0.96	5.4 \pm 2.5	8.6 \pm 0.9	0.0066 \pm 0.0035
12	0.52 \pm 0.21	11 \pm 5	6.2 \pm 0.7	0.0022 \pm 0.0012
13	0.70 \pm 0.28	9.7 \pm 4.4	8.0 \pm 0.8	0.0030 \pm 0.0016
14	2.42 \pm 0.97	46 \pm 20	9.2 \pm 1.0	0.0025 \pm 0.0013	2.75	2.34	1.24
15	1.07 \pm 0.43	15 \pm 7	6.0 \pm 0.6	0.0035 \pm 0.0019
16 ^f	0.29 \pm 0.12	59 \pm 28	6.6 \pm 0.7	0.00055 \pm 0.00029
Aperture radii = 114'' \simeq 6 \times (160 μ m PSF FWHM \simeq 260 pc)							
3	4.0 \pm 1.6	33 \pm 14	23.3 \pm 2.4	0.0050 \pm 0.0027	2.97	2.50	1.19
7	5.0 \pm 2.0	8.4 \pm 3.7	36.4 \pm 3.7	0.0030 \pm 0.0016	3.01	2.56	1.40
8	7.8 \pm 3.1	19 \pm 8.6	25.6 \pm 2.6	0.0040 \pm 0.0021	2.99	2.54	1.62
11	5.7 \pm 2.3	6.1 \pm 2.8	28.4 \pm 2.9	0.0048 \pm 0.0026
14	4.1 \pm 1.6	32 \pm 15	30.1 \pm 3.0	0.0016 \pm 0.00087	2.80	2.46	1.18
Total Galaxy							
NGC 6822	57 \pm 23	12.3 \pm 5.5	1340 \pm 140	0.00077 \pm 0.00043 ^g	3.34	2.88	1.55

^aSee Table 1 for source coordinates and cross-identifications.

^bCalculated using the relations presented in Dale & Helou (2002); uncertainties are estimated at the \sim 40% level.

^cCalculated as the unitless ratio of H α to TIR flux; ratios represent 1000 \times this fraction.

^dSee Table 4 for dust mass derivations; the values shown here are calculated using dust masses derived from the models of Draine & Li (2001), Li & Draine (2001, 2002), and Draine & Li (2006).

^eq_{TIR} is the “q” parameter evaluated using an estimate of the total IR luminosity ($\log(S(\text{TIR}/\text{Radio}))$); q₂₄ and q₇₀ are the monochromatic “q” parameters, as studied in Murphy et al. (2006).

^fNote that the local background surrounding region #16 in the MIPS images is very uncertain; see \S 3.1.1.

^gThis value uses the total H I mass from the entire system; using the H I mass contained in the matching aperture used for the global IR flux density extractions reduces the enclosed H I mass by \sim 10%.

rived for M51. While there is an appreciable scatter, it is clear that regions within NGC 6822 follow a different scaling between H α and 24 μ m luminosity than the regions in M51: the H II regions in NGC 6822 have much lower extinction than those in M51, as expected on the basis of the widely different metallicities (factor \sim 10-15; see Bresolin et al. 2004). Note that extinction corrections at H α will move points to the right in this plot, and cannot directly account for all of the observed dispersion (see further discussion in \S 3.1.1); we plot the largest detected reddening vector (0.75 mag, for aperture 7 or Hubble IV) in Figure 6 to demonstrate the severity of (spatially variable) extinction at H α . The scatter in this plot can then be interpreted as the effect of star formation on the local ISM. This expands the findings of Cannon et al. (2005, 2006), where the vigorously star-forming, metal-poor galaxies IC 2574 and NGC 1705 were also found to have different H α /24 μ m ratios than those found in more metal-rich galaxies. Further, it reiterates the conclusions of Kennicutt (1998): the infrared luminosity is a reliable SFR indicator only in metal-rich (i.e., dusty) environments, where a large fraction of the light from massive stars is reprocessed by dust to the infrared. We discuss these results further in \S 4.

3.2. Neutral Gas vs. Dust Emission

3.2.1. Correlations Between H I and Dust

The right column of Figure 4 shows the IR images overlaid with contours of H I column density at the 10^{21} cm⁻² level. It is clear from this image and Table 2 that the central disk of NGC 6822 is rich in neutral gas and has relatively small variations in H I column density over the apertures in this study (factor of \sim 2 variations in flux). Comparing the locations of H α , H I and dust emission in Figure 4, it is also clear that nearly all locations of active star formation (as evidenced by high-surface brightness H α emission) are associated with H I columns in excess of \sim 10²¹ cm⁻². Note by comparison with Figures 1 and 2, however, that the H I distribution is much more extended than the high-surface brightness optical body and the areas with strong FIR emission.

The surface brightness profiles of the FIR emission (see Figure 5) show that the 24 μ m emission is, in general, associated with local H I column density maxima. Moving toward cooler dust emission, the 70 and 160 μ m profiles show a much lower dynamic range than the 24 μ m profile; however, the peaks in the FIR nicely correlate with the locations of H I surface density maxima. For example, at radii of \sim 0.2, 1.0, and 1.6 kpc, the correlations

TABLE 4
DUST MASS DERIVATIONS IN NGC 6822

Region ^a	T _{DUST} ^b (K)	Blackbody Dust Mass ^b (10 ³ M _⊙)	α ^c	Dale et al. Dust Mass ^c (10 ³ M _⊙)	Li & Draine Dust Mass ^d (10 ³ M _⊙)
Aperture radii = 57'' = 3 × (160 μm PSF FWHM) ≳ 130 pc					
1	21 ± 2	1.4 ± 0.7	2.03	12.6 ± 6.3	2.81 ± 1.40
2	21 ± 2	1.6 ± 0.8	2.88	14.4 ± 7.2	3.11 ± 1.55
3	24 ± 2	1.6 ± 0.8	2.31	14.4 ± 7.2	3.27 ± 1.63
4	22 ± 2	1.3 ± 0.6	2.75	11.7 ± 5.9	3.26 ± 1.63
5	23 ± 2	0.82 ± 0.41	2.00	7.4 ± 3.7	2.11 ± 1.05
6	21 ± 2	1.4 ± 0.7	2.81	12.6 ± 6.3	2.63 ± 1.31
7	24 ± 2	2.1 ± 1.1	2.00	18.9 ± 9.5	4.62 ± 2.31
8	25 ± 2	2.3 ± 1.1	1.72	20.7 ± 10.4	5.79 ± 2.89
9	23 ± 2	0.97 ± 0.49	2.62	8.7 ± 4.4	2.04 ± 1.02
10	24 ± 2	0.66 ± 0.33	2.50	5.9 ± 3.0	1.01 ± 0.50
11	23 ± 2	2.6 ± 1.3	2.56	23.4 ± 11.7	5.61 ± 2.80
12	21 ± 2	0.93 ± 0.47	2.75	8.4 ± 4.2	1.40 ± 0.70
13	21 ± 2	1.1 ± 0.6	2.81	9.9 ± 5.0	2.43 ± 1.21
14	25 ± 2	1.3 ± 0.6	2.03	11.7 ± 5.9	2.31 ± 1.15
15	23 ± 2	0.98 ± 0.49	2.19	8.8 ± 4.4	2.09 ± 1.04
16 ^e	24 ± 2	0.23 ± 0.12	2.50	20.7 ± 10.4	0.36 ± 0.18
Aperture radii = 114'' = 6 × (160 μm PSF FWHM) ≳ 260 pc					
3	23 ± 2	4.7 ± 2.3	2.56	42.3 ± 21.2	11.7 ± 5.9
7	24 ± 2	4.7 ± 2.3	2.28	42.3 ± 21.2	11.1 ± 5.5
8	25 ± 2	4.7 ± 2.3	1.91	42.3 ± 21.2	10.2 ± 5.1
11	23 ± 2	6.7 ± 3.3	2.62	60.3 ± 30.2	13.6 ± 6.8
14	25 ± 2	2.8 ± 1.4	2.25	25.2 ± 12.6	4.91 ± 2.4
Total Galaxy					
NGC 6822	23 ± 2	83 ± 42	2.56	750 ± 380	103 ± 52

^aSee Table 1 for source coordinates and cross-identifications.

^bAverage dust temperature and implied dust mass over the aperture, derived by blackbody fitting.

^cα and dust mass values derived using the semiempirical SED models of Dale et al. (2001) and Dale & Helou (2002); typical errors on the α index are ∼ 0.15 (see discussion in § 3.2.2).

^dDust mass derived using the SED models of Draine & Li (2001), Li & Draine (2001, 2002), and Draine & Li (2006).

^eNote that the local background surrounding region #16 in the IR images is very uncertain; see § 3.1.1.

between H I, Hα and IR emission are especially strong (though relative variations are evident).

To further quantify the correlation between H I and FIR emission, Figures 7 and 8 show pixel-by-pixel histograms and scatter plot comparisons of H I column density vs. surface brightness measurements in the Hα and IR bands. These plots were created by comparing H I, Hα, and IR surface brightnesses on an individual pixel basis. They clearly demonstrate that FIR and Hα emission are strongly peaked in regions with H I column densities ≳ 10²¹ cm⁻². The 70 and 160 μm histograms show that the regions of strongest dust emission (as traced by very high-surface brightness 70 and 160 μm emission; thin gray lines in Figure 7) are associated with the highest H I column densities: the histogram at 16 MJy sr⁻¹ shows a median value ∼ 50% higher than the median at 4 MJy sr⁻¹. There is little difference in the pixel-by-pixel distribution of surface brightnesses at Hα or in the IR bands; above H I columns of ∼ 5 × 10²⁰, the nebular and dust emission both increase in strength as the H I column increases, with the highest-surface brightness emission strongly peaked in regions with H I column densities ≳ 10²¹ cm⁻².

We now consider the origin of the evident correlation between nebular and IR surface brightness as a function

of H I column density. If the strength of the dust emission is correlated primarily with dust heating, then the far-IR colors should become warmer as the ratio of dust to H I emission increases. However, if the strength of the dust emission is related to an increase in the density of dust, then the ratio of infrared to H I emission will not be correlated with the far-infrared colors. To investigate this scenario, we plot in Figure 9 the ratios of S₇₀/S_{H I} and S₁₆₀/S_{H I} for the regions listed in Table 1, each as a function of IR color [here, Log(S₇₀/S₁₆₀)]. These plots allow us to gauge how much IR emission is arising per unit H I mass at a given dust temperature (or, similarly, at a given radiation field strength level). It is clear from Figure 9(a) that as the IR color increases (radiation field strength rising), the amount of 70 μm emission per unit H I mass also increases. At 160 μm, this correlation is less evident, suggesting that 70 μm emission is more sensitive to local heating, as one would expect for thermal emission in the temperature range of interstellar dust (see also Dale et al. 2005). This arises in part due to the 70 μm band falling near the transition point between the hot dust emission that dominates shorter wavelengths and the ∼ 20–30 K dust emission that radiates at longer wavelengths. While the errorbars in both plots are large, we can infer that localized heating of dust, in addition to

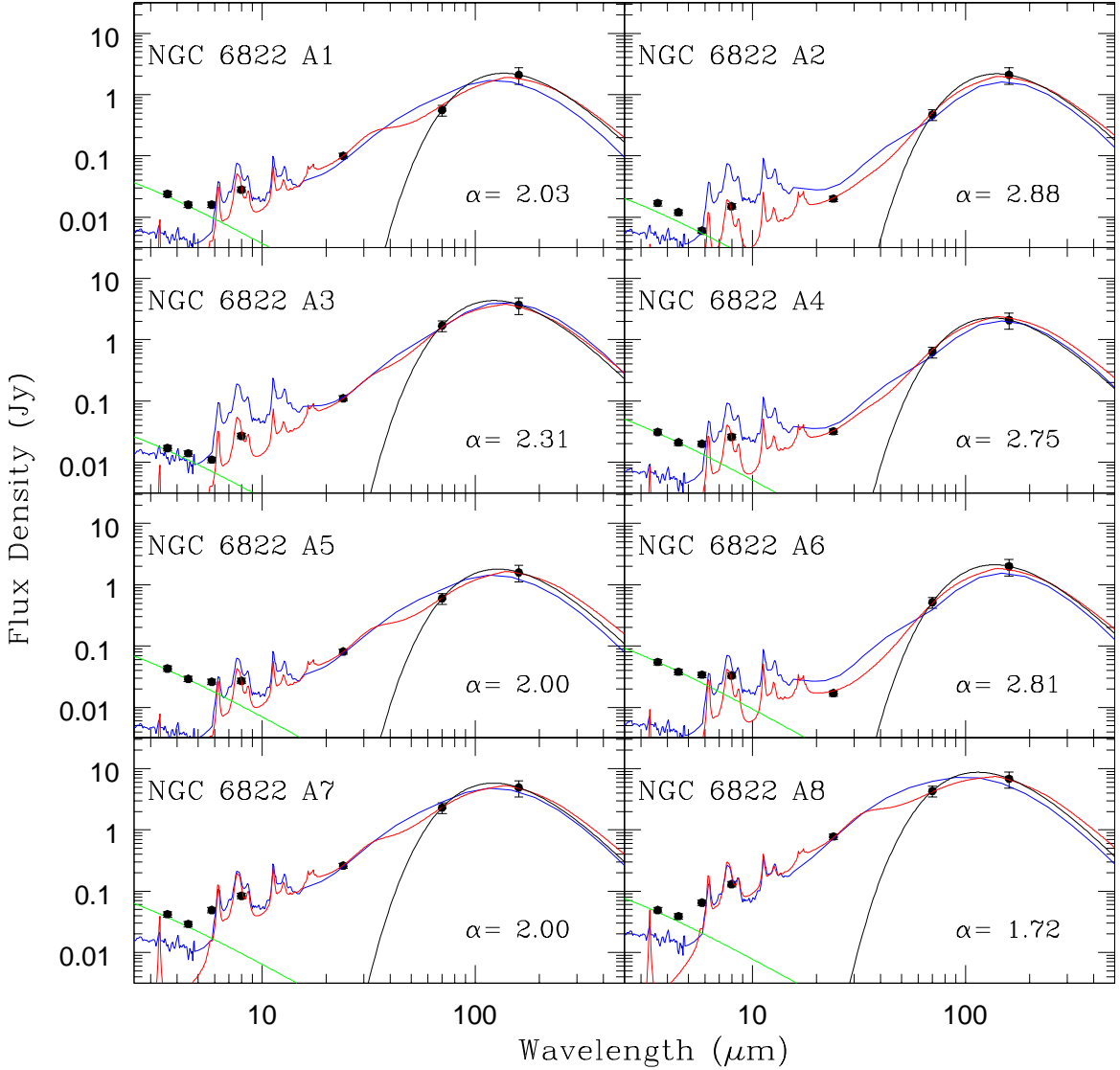


FIG. 10.— Modified blackbody and SED model fits to the observed data for apertures A1–A8 (see Table 1 and Figure 3). Each panel shows the observed infrared flux densities, overlaid with: a single-temperature modified blackbody fit to the observed 70 and 160 μm flux densities (fits shown in black); the SED models of Dale & Helou (2002), fitting to the observed 24, 70 and 160 μm flux densities (fits shown in blue); the models of Li & Draine (2001, 2002) and Draine & Li (2006), fitting to all observed flux densities longward of 5 μm (fits shown in red); and a stellar component based on population synthesis models, fit to the 3.6 and 4.5 μm bands (green line). Note that single-temperature modified blackbody fits strongly underestimate the observed 24 μm flux densities in all cases. The value of α from the Dale & Helou (2002) fits is shown at the bottom right of each panel.

increased H I column density, plays an important role in controlling the nature of IR emission. The different dynamic ranges of nebular, dust and H I emission may also suggest increasing H I columns due to photodissociation of H_2 in regions of active star formation.

The simplest physical scenario that explains these observational trends is one where the H I and dust are mixed in the ISM, and that as the local radiation field strength increases, so does the total IR emission per unit dust mass (e.g., Dale et al. 1999). If the increase in the dust emission surface brightness was due solely to an increase in the local H I column density (i.e., a relatively constant-strength interstellar radiation field producing higher surface brightnesses in regions of larger H I columns), then the dynamic range of the dust emission would be expected to be similar to that in H I. How-

ever, Figures 7 and 8 clearly show a large scatter of IR flux densities at a given H I column or a given radiation field strength. We caution that with the present observations, it is not possible to assure that the H I, $\text{H}\alpha$ and IR observations are all sampling interstellar media that are exactly co-spatial; however, the clear correlations between these various phases (see Figures 4, 7 and 8) suggest that dust absorption and re-radiation are closely tied to local star formation intensity. Note that no regions with high IR surface brightness and high H I column density are $\text{H}\alpha$ -deficient (i.e., non-detections); this again supports the theory that local star formation is an important mechanism in the production of the observed IR SED.

3.2.2. Derivation of Dust Masses

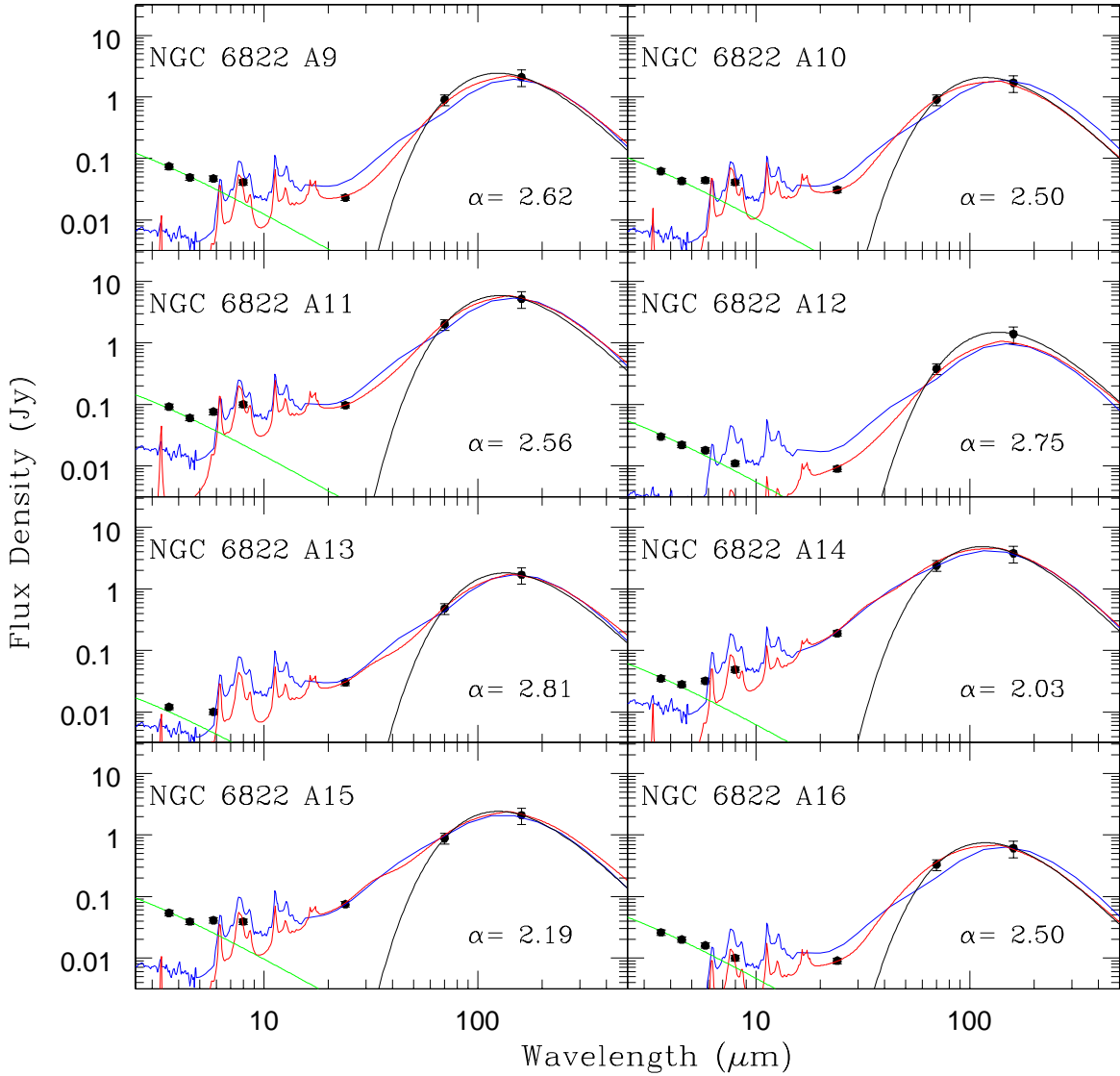


FIG. 11.— Same as Figure 10, but for apertures A9–A16.

In the following, we calculate the dust mass of NGC 6822 (both globally and within the apertures shown in Figure 3) using three different methods of increasing sophistication. We begin with a single-temperature fit, and discuss explicitly the shortcomings of such an approach in accurately representing the observed SEDs within NGC 6822. We then discuss two SED modeling techniques that offer a more physical representation of the data.

First, we apply a simple single-temperature modified blackbody fit to the data (see, e.g., Hildebrand 1983; Bianchi et al. 1999). Dust mass values are derived via the following equation:

$$M_{dust} = \frac{D^2 f_\nu}{\kappa_\nu B(T)} \quad (3)$$

where D is the distance to the galaxy, f_ν is the flux density, κ_ν represents the absorption opacity of the dust (given in Li & Draine 2001), and $B(T)$ is the Planck function evaluated at temperature T , derived by fitting

a blackbody modified by a λ^{-2} emissivity function to the 70 and 160 μm data. Using this method, we derive a total dust mass of $(8.3 \pm 4.2) \times 10^4 M_\odot$; Table 4 shows the inferred dust masses for each region.

This simple prescription assumes that all the IR emission in a galaxy is at both the same temperature and in thermal equilibrium. A combination of the composite nature of IR emission [arising from large grains, polycyclic aromatic hydrocarbons (PAH), very small grains, etc.], the stochastic heating processes that are of differing importance for various types of grains (see Draine & Li 2001 for a detailed discussion), and the complex relations between dust emission, gas density, and the local interstellar radiation field, suggests that this single-temperature assumption is likely incorrect, at least on local scales. Indeed, Figures 10, 11 and 12 show that the simple blackbody fits to the 70 and 160 μm data are not intended to represent the hot dust emission at shorter wavelengths; the fits fall short of the observed 24 μm data points by orders of magnitude. Given these

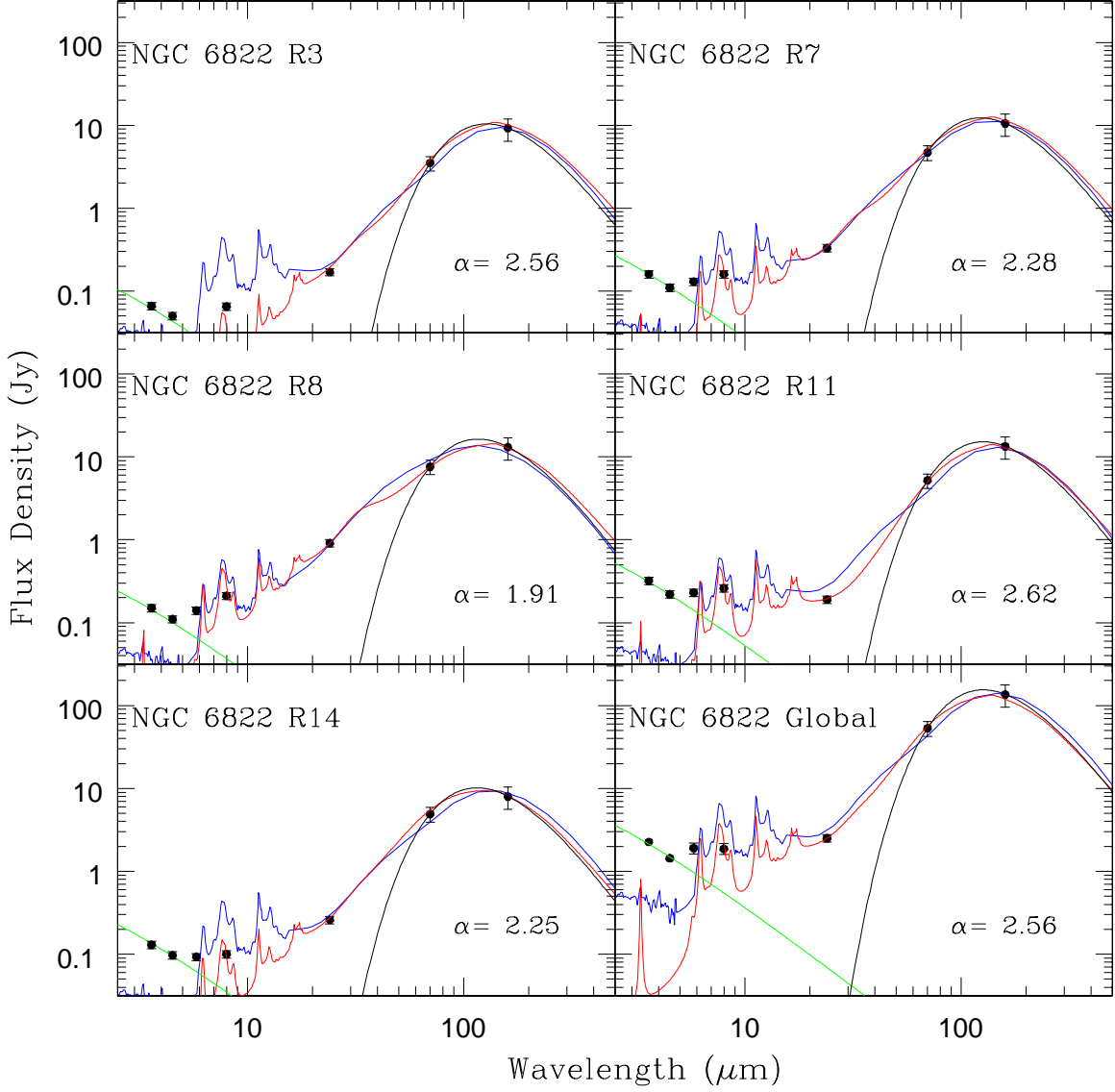


FIG. 12.— Same as Figure 10, but for the apertures with expanded radii (see Table 2) and for the global SED of NGC 6822. Note that the y-axis has been increased compared to Figures 10 and 11.

failures, we seek a more detailed treatment of the SEDs that accounts for the potential contribution of multiple grain populations to the dust mass.

A second and more robust method with which to calculate the dust mass using IR to submillimeter data is with the SED models presented by Dale et al. (2001) and Dale & Helou (2002). These models assume that large grains, very small grains, and PAH molecules contribute to the integrated IR energy budget in a galaxy. Semiempirical SEDs are constructed assuming a power-law distribution of dust mass as a function of the strength of the local interstellar radiation field (U). With U normalized to unity for the radiation field near the sun, masses are computed via the relation:

$$dM_{dust}(U) \propto U^{-\alpha} dU \quad (4)$$

where M_{dust} is the dust mass heated by a radiation field of strength $\leq U$, and α represents the relative contributions of the different local SEDs. The fitted values of α correlate with an empirical measure of the

ratio $\text{Log}[f_{\nu}(60\mu\text{m})/f_{\nu}(100\mu\text{m})]$, which was calibrated against *IRAS* data (see Dale et al. 2001; Dale & Helou 2002). This ratio then corresponds to a scaling factor by which the dust mass estimates using single-temperature blackbody fits (see above) should be increased to account for mass components not well-constrained by the blackbody fit (see application of this method to NGC 7331 in Regan et al. 2004). Values of α between ~ 2 –4 imply a mass increase of a factor of 9 (see Figure 6 of Dale & Helou 2002); α values less than this show a smaller increase in dust mass (e.g., $\alpha = 1.75$ corresponds to a factor of ~ 8 increase).

Fitting these models to the flux densities of the regions and the entire galaxy (see Tables 2 and 4) yields values of $2.0 \lesssim \alpha \lesssim 2.8$ for nearly all regions; Monte Carlo simulations of the errors on the index α were performed during the fitting of these models to 68 galaxies in Dale et al. (2005), providing typical errors of ~ 0.15 . The observed values of α in NGC 6822 are consistent with those seen

in the Dale et al. sample; the only exception is region 8 (Hubble V), the strongest IR, H α and radio continuum source in the galaxy. This active star formation region may have a strong enough local radiation field that a large component of cool grains (which would lead to a pronounced mass increase) is absent. Figures 10, 11 and 12 show these model fits to each region, and Table 4 gives the values of α for each fit and the inferred dust mass using these SED models. Given the uncertainties in the dust masses derived from the blackbody fits (see above and Table 4) and the varying quality of the least-squares fit for each region (compare, e.g., the fits for regions 6 and 14), all regions are consistent with an increase in mass by a factor of ~ 9 ; the global dust mass increases accordingly to $(7.5 \pm 3.8) \times 10^5 M_{\odot}$.

A third and yet more sophisticated estimate of the dust mass in the galaxy can be found using the models of Li & Draine (2001, 2002) and (Draine & Li 2006). Here, radiation field strengths are varied via power-law distributions; PAH, silicate and graphite grains are illuminated and the resulting SEDs can be compared to the observations. The fit of these models to our observations is also shown in Figures 10–12. The observed SEDs are well-reproduced by these models, when a small fraction (~ 5 –30%, depending on the individual region) of the dust mass is exposed to radiation fields largely in excess of the local average (see Draine & Li 2006). The implied dust masses are given in Tables 3 and 4; these masses are smaller than those derived using the Dale et al. (2001) and Dale & Helou (2002) models. The derived global dust mass is $(1.03 \pm 0.52) \times 10^5 M_{\odot}$.

We note that our global flux densities produce SEDs that are in good agreement with the fluxes measured in Israel et al. (1996). Our use of sophisticated SED modeling techniques [Dale et al. (2001) and Dale & Helou (2002); Li & Draine (2001, 2002) and Draine & Li (2006)] results in dust masses that are larger than those derived by Israel et al. (1996). These differences are thus attributable solely to our different (and likely more physical) modeling approach.

Note that our data may remain insensitive to a potential component of very cold dust (which may be located away from regions of star formation). Previous studies (e.g., Eales et al. 1989, Devereux & Young 1990, Kwan et al. 1992, and Calzetti et al. 2000) have shown that observations from the mid-IR into the sub-millimeter regime are needed to fully quantify the range of dust temperatures, grain sizes, and opacities, and to provide a robust estimate of the total dust mass in a galaxy. Popescu et al. (2002), for example, noted that ~ 15 –20 K dust may be present in many nearby galaxies. Data longward of $160 \mu\text{m}$ would be needed to determine whether such dust is present in NGC 6822. Some observational results have also demonstrated that dust with temperatures as cold as 5–10 K (e.g., Madden et al. 2002; Galliano et al. 2003, 2005) may be present in dwarf galaxies. However, theoretical research (e.g., Li 2004) and other observational results (Dumke et al. 2004; Bendo et al. 2006, e.g.) have suggested that 5–10 K dust temperatures would require physically implausible dust grain properties or unrealistically high dust masses. Nonetheless, if dust cooler than 20 K exists in NGC 6822, then these data may afford only a lower limit on the total dust content of the system.

3.2.3. The Empirical Dust-to-H I Ratio

The *Spitzer* images of NGC 6822 can be compared to our sensitive H I imaging to study the dust-to-gas ratio at ~ 130 pc resolution. We define the dust-to-gas ratio (hereafter represented as \mathcal{D}) as the ratio of dust mass (as traced by these *Spitzer* observations) to H I mass; no correction is applied for the (uncertain) contribution of CO or H $_2$ gas. At sub-solar metallicities (recall that NGC 6822 has a metallicity $\simeq 30\% Z_{\odot}$), the molecular phase of the ISM is different from that in more metal-rich systems. Theoretical predictions (e.g. Maloney & Black 1988; Bolatto et al. 1999) and observational evidence (e.g., Taylor et al. 1998; Leroy et al. 2005) have shown that CO clouds have a smaller volume filling factor in metal-poor systems than in spiral galaxies. Israel (1997) uses CO observations of selected regions in NGC 6822 to infer a total molecular mass $\sim 10\%$ of the H I mass (though these numbers are highly uncertain, depending on the conversion factor used to infer total H $_2$ content from observed CO intensities). Since a complete census of the molecular material in NGC 6822 is difficult, we simply study the relation of dust and H I gas; any molecular material in NGC 6822 will lower the derived \mathcal{D} .

Throughout the disk, the mean value of \mathcal{D} (in apertures of physical radius ~ 130 pc, using the dust masses derived from the models of Li & Draine) is ~ 0.004 (with little change when using apertures with 4 times larger area; see Tables 3 and 4). Variations of a factor ~ 3 are seen among individual regions, and the errors on the \mathcal{D} values are also high (arising from the relatively uncertain dust mass estimates). These average values are lower than the average global values found for other *SINGS* galaxies using similar modeling techniques. For example, Draine et al. (2006, in preparation) present detailed dust mass estimates for many *SINGS* galaxies: for 40 systems with *Spitzer* data but no submillimeter observations, the average global \mathcal{D} (excluding dwarf galaxies and the contribution of molecular hydrogen) is $M_{\text{dust}}/M_{\text{HI}}=0.02$; i.e. a factor of ~ 5 higher than the average local ratios found using the same models in NGC 6822.

Israel et al. (1996) finds a global \mathcal{D} of 1.4×10^{-4} in NGC 6822 using *IRAS* data; our derived global value (using the Li & Draine models) is $\sim 8 \times 10^{-4}$ (see Table 3). Our *Spitzer* data recover very similar global flux densities as found in the Israel et al. (1996) study; the differences in dust mass and \mathcal{D} are attributed to the use of detailed SED models of the IR emission. Note that all of the \mathcal{D} values derived for the apertures listed in Table 4 are higher than the global value. This is expected since the dust is strongly peaked in regions of high H I column and star formation (e.g., see Figures 5, 7 and 8), but the bulk of the extended H I distribution has little associated dust emission (see Figure 2). Recall, however, that our data remain insensitive to a potential component of very cold dust (see more detailed discussion above).

We note by examining the individual panels of Figures 10, 11 and 12 that the model fits to the IR SEDs predict significant power in the PAH bands between ~ 5 and $20 \mu\text{m}$ (though see discussion of potential metallicity effects in Dale et al. 2005). Most regions show a rise in the SED moving from $4.5 \mu\text{m}$ to 5.8 and $8.0 \mu\text{m}$, part or all of which may be associated with aromatic band

emission in the ISM. Given the metallicity of NGC 6822 ($Z \simeq 30\% Z_{\odot}$) and the empirical dependence of PAH emission on metallicity Engelbracht et al. (2005), it will be fruitful to compare the IRAC images with IRS spectra of various regions in NGC 6822. Initial results of *SINGS* extra-nuclear IRS spectra of the major star formation complexes (e.g., Hubble I/III, V, X) show that PAH emission is prominent throughout the galaxy. This will allow a proper spatial and spectral decomposition of PAH emission in the metal-poor ISM at unprecedented resolution.

3.3. The Radio - Far-IR Correlation

In normal star-forming galaxies, there is a remarkably tight correlation between the total IR luminosity and the strength of radio continuum emission (see, e.g., de Jong et al. 1985, Helou et al. 1985, Condon 1992, and references therein). Given the differing physical mechanisms giving rise to far-IR and radio emission, the tightness of the relation (scatter of less than 0.3 dex over multiple orders of magnitude in luminosity) is especially remarkable. Bell (2003) shows that the relation holds for dwarf galaxies, which are generally deficient both in IR and radio emission with respect to massive galaxies, when the emission is normalized by the star formation rate. However, these systems require a complex interplay of star formation, dust content and magnetic fields to produce the apparently linear relation in this regime.

Figure 3(h) shows that only sources 2, 3, 4, 7, 8, and 14 are detected at high S/N in our radio continuum imaging. These are the six highest-surface brightness H α regions in the galaxy. We tentatively detect lower surface brightness regions throughout the disk, but the presence of strong background sources precludes us from analyzing them with confidence. Flux densities for these regions are quoted as upper limits in Table 2. Assuming that the monochromatic or TIR fluxes and the radio continuum emission are related via constant values [$q \propto \log(S_{\text{IR}}/S_{\text{RC}})$; see Bell (2003) and Murphy et al. (2006a) for details], we calculate two values of “q”. The first is a monochromatic comparison of the IR and radio continuum flux densities:

$$q_{\lambda} (\mu\text{m}) = \log \frac{f_{\nu}(\lambda)(Jy)}{f_{\nu}(20\text{cm})(Jy)} \quad (5)$$

The second compares a measure of the total infrared flux with the radio continuum:

$$q_{\text{TIR}} = \log \frac{\text{TIR}}{(3.75E12 W m^2)} - \log \frac{S_{1.4\text{GHz}}}{(W m^2 Hz)} \quad (6)$$

We calculate “q” (see Table 3) in individual regions, as well as throughout the total galaxy. The resulting values are in excellent agreement with those found both locally and globally in larger samples of galaxies. For example, Bell (2003) finds a median global $q_{\text{TIR}} = 2.64 \pm 0.02$ in a sample of more than 200 galaxies. Murphy et al. (2006a) explores the radio-IR correlation on a spatially resolved basis (sampling physical regions of ~ 300 – 750 pc) using *SINGS* data on four nearby spiral galaxies, finding ranges of $0.85 \lesssim q_{24} \lesssim 1.10$ and $1.95 \lesssim q_{70} \lesssim 2.25$ (where q_{24} and q_{70} are the monochromatic “q” parameters derived using equation 5). In NGC 6822, there is slight evidence that regions with a high H α /TIR ratio show lower “q” values;

there is no evidence for a trend of “q” with \mathcal{D} or with TIR flux.

The agreement of the local and global values with the canonical radio-IR relations derived for spiral galaxies suggests that both the radio and IR are significantly depleted in NGC 6822, conspiring to produce the observed “q” parameters. Different physical mechanisms appear to be at work in the ISM of this dwarf galaxy compared to those operating in the ISM of more massive spirals. In NGC 6822, the bulk of the radio emission appears to be thermal: in § 3.1.1, we showed that most regions have thermal fractions $>90\%$ (the strongest nonthermal sources are regions 7 and 8, with thermal fractions of $\sim 50\%$ and 70% , respectively). In contrast, nonthermal processes produce the bulk of radio continuum emission in massive spiral galaxies [see Murphy et al. (2006a) and Murphy et al. (2006b) for more detailed discussions of the radio-FIR correlation in *SINGS* galaxies]. Evidently, in NGC 6822 the IR emission per unit star formation is reduced by about the ratio of free-free/nonthermal emission in normal spirals, conspiring to produce the observed “q” values.

The relative ratios of radio and IR emission strengths in NGC 6822 are in marked contrast to the strong deviations from the canonical radio-IR relation found for very active low-metallicity galaxies in the *SINGS* sample. Cannon et al. (2005, 2006) show that the radio-FIR correlation breaks down in very strongly star forming regions. The “supergiant shell” region of IC 2574 has induced strong variations of the “q” parameter (over an order of magnitude); the dwarf starburst galaxy NGC 1705 shows strong FIR emission but is a radio non-detection. Other types of galaxies can also be extremely radio-deficient, though likely for different reasons than those seen in NGC 6822 [see, e.g., the Roussel et al. (2006) study of the nascent starburst in the lenticular galaxy NGC 1377].

These results suggest that star formation intensity has a dramatic effect both on the appearance of radio continuum emission, and on the derived correlation between FIR emission and radio continuum luminosity, in galaxies with small potential wells (for comparison, note that more massive starburst galaxies in the Bell 2003 sample show little deviation from the derived radio-TIR relation). The intensity of star formation relative to the presence of a stable large-scale disk is important, since the ratio of activity to disk density and gravity will govern the amount of disruption and blow-out that takes place (thus, the irregular nature of NGC 6822 is likely also important in determining the ratio of IR to radio emission). The relatively uniform values of “q” found in larger spiral galaxies and quiescent dwarfs argues that disk disruption by star formation is minimal; the strongly varying values of “q” in starbursting dwarfs suggests that the small disks are being overwhelmed by the star formation activity.

4. DISCUSSION AND CONCLUSIONS

We have presented IR observations of the Local Group dwarf irregular galaxy NGC 6822 obtained with *Spitzer* as part of *SINGS*. The galaxy is highly resolved at all imaging bands; the resolution limit is driven by the FWHM of the $160 \mu\text{m}$ PSF. At ~ 130 pc physical resolution, we study the nature of FIR emission and compare

to observations in the optical and radio. These sensitive data reveal a wealth of structure within the galaxy. Our study confirms some previous results, while also offering new insights into the nature of infrared emission in the metal-poor ISM. We discuss these topics in more detail below.

The total monochromatic FIR flux densities are found to be $S_{24} = 2.51 \pm 0.50$ Jy; $S_{70} = 53.2 \pm 15$ Jy; $S_{160} = 136.2 \pm 40$ Jy. SED model fits to these data allow comparison with previous *IRAS* flux measurements; our *Spitzer* flux densities are in excellent agreement with the measurements in Israel et al. (1996). Using the relations presented in Dale & Helou (2002), these global flux densities correspond to a total IR flux of $\sim 5.7 \times 10^{-12}$ W m $^{-2}$ ($\sim 4.3 \times 10^7 L_{\odot}$).

IR emission at 24, 70 and 160 μm is found only within the central, high-H I column density ($\gtrsim 10^{21}$ cm $^{-2}$) region of NGC 6822. The total H I distribution is much more extended than the high-surface brightness stellar or dust emission components. The 24 μm surface brightness profile closely traces that of H α , delineating regions of ongoing star formation. The profiles of 70 and 160 μm emission also trace local H I column density maxima.

Comparing (monochromatic and total) FIR emission with a sensitive H α image reveals a strong morphological correlation between IR and H α surface brightness; here we are directly observing the re-processing of photons by dust. Roughly 50% of the TIR flux is attributable to discrete FIR sources, all of which have at least a low-level H α counterpart; the remaining FIR emission arises from a “diffuse” component of the ISM (slightly stronger at 70 and 160 μm than at 24 μm ; see detailed discussion in § 3.1.1) that is apparently not associated with massive star formation. Gallagher et al. (1991) and Israel et al. (1996) find similar results from *IRAS* imaging of NGC 6822; we interpret this as the re-processing of non-ionizing photons in the ISM or as the escape of radiation from the star formation regions.

We find variations in the relative ratios of nebular and dust continuum emission. While differential extinction can cause some of the observed fluctuations, it cannot account for the full breadth of properties seen in the galaxy. Using *SINGS* observations of the starbursting dwarf galaxies IC 2574 and NGC 1705, Cannon et al. (2005, 2006) found similar variations and attributed them to the direct impact of recent star formation on the local ISM (i.e., production and re-processing of photons). The results presented here extend this trend to more typical, quiescent dwarfs.

Evidence is mounting from spatially resolved *Spitzer* observations of dwarf galaxies that these systems follow a different trend of 24 μm vs. H α luminosity than what is seen in more metal-rich systems (see, e.g., Calzetti et al. 2005). This result is in agreement with previous observations of dwarf galaxies (e.g., Hunter et al. 1989). Two different scenarios can account for this observational trend. The first one, physically simple and more commonly used, is related to the low dust content of low-metallicity galaxies. Here, low-metallicity galaxies simply do not have enough metals to form dust in the same fraction as more metal rich environments. The second scenario posits that dwarfs harbor massive components of cold dust ($T \sim 5\text{--}10$ K) that is simply not heated by ongoing star formation. Such dust would peak past 200

μm and remain undetected in the present *Spitzer* observations, contributing to part of the observed discrepancy; observational evidence exists both for and against such a component in nearby galaxies (see detailed discussion in § 3.2.2). Clearly, sensitive observations of a large sample of dwarf galaxies between 200 and 1000 μm are needed to address this issue.

As mentioned previously, our global flux densities for NGC 6822 are in good agreement with those from Israel et al. (1996). We use sophisticated SED modeling techniques [Dale et al. (2001) and Dale & Helou (2002); Li & Draine (2001, 2002) and Draine & Li (2006)] to derive dust masses that are higher than those derived by Israel et al. (1996). The differences in mass are thus attributable solely to our more physical modeling approach, which takes into account the variety of dust species and heating levels in each region within the disk (see detailed discussion in § 3.2.2). For a given TIR luminosity, our models recover a higher dust mass than simple blackbody fits (see detailed discussion in § 3.2.2). The treatment of multiple grain populations likely means that the increased dust masses are a better representation of the mass radiating between 10 and 160 μm . Using these techniques, we derive a total dust mass of $\sim 10^5 M_{\odot}$ (this value is derived using the Li & Draine models).

Comparing to our high-resolution H I imaging, we can explore the mass ratio of warm dust to H I gas (\mathcal{D}) in the ISM. Given the low nebular abundance of the system ($Z \simeq 30\% Z_{\odot}$), we can thus provide constraints on a potential trend of \mathcal{D} with abundance. Metal-poor dwarf galaxies might be expected to have a lower \mathcal{D} (i.e., higher gas mass fraction) than more metal-rich galaxies such as the Milky Way (e.g., Thronson & Telesco 1986). Lisenfeld & Ferrara (1998) have argued that dwarf irregular galaxies have a clear relation between these two quantities in a global sense (using dust masses derived from single-temperature blackbody fits).

Here, we derive a global $\mathcal{D} \simeq 8 \times 10^{-4}$. This is ~ 25 times lower than the average global values found in the new *SINGS* study of Draine et al. (2006, in prep.), wherein dust masses are calculated for a large sample of galaxies (excluding dwarfs). On local scales (~ 130 pc), the dust mass per unit H I mass is higher (by a factor of ~ 5), though still lower than the global values found by Draine et al.

We propose a simple model for the relative ratios of dust mass to H I mass in the ISM. As noted above, dwarf galaxies may contain large reservoirs of cold dust ($T \sim 5\text{--}10$ K) that are undetectable with *Spitzer* observations (e.g. Madden 2002; Galliano et al. 2005). Note, however, that the dilution of the radiation field required for this dust to remain at such low temperatures may require it to be located at large distances from the star formation regions and thus essentially decoupled from the active ISM (note that other mechanisms may also be important in dwarfs, including dust destruction by supernova shocks; see, e.g., Bot et al. 2004). Superposed on this putative cool component are regions radiating between 10 and 160 μm ; here, photons are being absorbed and re-radiated as IR photons. The low dust contents of metal-poor galaxies plays an important role in the microphysics of this process. Galaxies with widespread, elevated star formation will heat more of their total dust component than more quiescent systems. When more sensitive observa-

tions are possible between 200 and 1000 μm , we will be able to quantify the relative masses of these components in low-mass dwarf galaxies.

Finally, it is interesting that NGC 6822 seems to fall near the canonical measures of the radio-FIR relation (e.g., Bell 2003; Murphy et al. 2006a). 20 cm radio continuum imaging reveals six high surface brightness sources, each of which appears to be of thermal origin. The monochromatic and total IR “q” parameters are similar to those found for more massive galaxies. This agreement is interesting, given that nonthermal emission dominates the radio continua of spiral disks. The simplest explanation is that depleted radio and far-IR emission strengths conspire to produce the observed values. These findings in NGC 6822 are in marked contrast to recent results for very active star-forming dwarf galaxies, where significant deviations from the canonical radio-FIR relation are found (Cannon et al. 2005, 2006). Taken to-

gether, these data suggest that star formation intensity is one of the important parameters that governs the observed radio-FIR relation in dwarf galaxies.

Support for this work, part of the *Spitzer Space Telescope* Legacy Science Program “The Spitzer Nearby Galaxies Survey,” was provided by NASA through contract 1224769 issued by JPL/Caltech under NASA contract 1407. The authors thank the anonymous referee for a constructive review, and Henry Lee for providing optical spectroscopy results prior to publication. This research has made use of the NASA/IPAC Extragalactic Database (NED) which is operated by the Jet Propulsion Laboratory, California Institute of Technology, under contract with the National Aeronautics and Space Administration, and NASA’s Astrophysics Data System.

REFERENCES

- Babul, A., & Ferguson, H. C. 1996, *ApJ*, 458, 100
 Bell, E. F. 2003, *ApJ*, 586, 794
 Bendo, G. J., et al. 2006, *ApJ*, in press (astro-ph/0607669)
 Bianchi, S., Davies, J. I., & Alton, P. B. 1999, *A&A*, 344, L1
 Bolatto, A. D., Jackson, J. M., & Ingalls, J. G. 1999, *ApJ*, 513, 275
 Bot, C., Boulanger, F., Lagache, G., Cambr esy, L., & Egret, D. 2004, *A&A*, 423, 567
 Bresolin, F., Garnett, D. R., & Kennicutt, R. C., Jr. 2004, *ApJ*, 615, 228
 Calzetti, D., Armus, L., Bohlin, R. C., Kinney, A. L., Koornneef, J., & Storchi-Bergmann, T. 2000, *ApJ*, 533, 682
 Calzetti, D., et al. 2005, *ApJ*, 633, 871
 Cannon, J. M., et al. 2005, *ApJ*, 630, L37
 Cannon, J. M., et al. 2006, *ApJ*, 647, 293
 Caplan, J., & Deharveng, L. 1986, *A&A*, 155, 297
 Chy zy, K. T., Knapik, J., Bomans, D. J., Klein, U., Beck, R., Soida, M., & Urbanik, M. 2003, *A&A*, 405, 513
 Condon, J. J. 1987, *ApJS*, 65, 485
 Condon, J. J. 1992, *ARA&A*, 30, 575
 Dale, D. A., Helou, G., Silberman, N. A., Contursi, A., Malhotra, S., & Rubin, R. H. 1999, *AJ*, 118, 2055
 Dale, D. A., et al. 2000, *AJ*, 120, 583
 Dale, D. A., Helou, G., Contursi, A., Silberman, N. A., & Kolhatkar, S. 2001, *ApJ*, 549, 215
 Dale, D. A., & Helou, G. 2002, *ApJ*, 576, 159
 Dale, D. A., et al. 2005, *ApJ*, 633, 857
 de Blok, W. J. G., & Walter, F. 2000, *ApJ*, 537, L95
 de Blok, W. J. G., & Walter, F. 2003, *MNRAS*, 341, L39
 de Blok, W. J. G., & Walter, F. 2006, *AJ*, 131, 343
 de Jong, T., Klein, U., Wielebinski, R., & Wunderlich, E. 1985, *A&A*, 147, L6
 Devereux, N. A., & Young, J. S. 1990, *ApJ*, 359, 42
 Draine, B. T., & Li, A. 2001, *ApJ*, 551, 807
 Draine, B. T., & Li, A. 2006, *ApJ*, submitted (astro-ph/0608003)
 Dumke, M., Krause, M., & Wielebinski, R. 2004, *A&A*, 414, 475
 Eales, S. A., Wynn-Williams, C. G., & Duncan, W. D. 1989, *ApJ*, 339, 859
 Ellis, R. S. 1997, *ARA&A*, 35, 389
 Engelbracht, C. W., et al. 2004, *ApJS*, 154, 248
 Engelbracht, C. W., Gordon, K. D., Rieke, G. H., Werner, M. W., Dale, D. A., & Latter, W. B. 2005, *ApJ*, 628, L29
 Fazio, G. G., et al. 2004, *ApJS*, 154, 10
 Gallagher, J. S., Hunter, D. A., Gillett, F. C., & Rice, W. L. 1991, *ApJ*, 371, 142
 Gallart, C., Aparicio, A., & Vilchez, J. M. 1996a, *AJ*, 112, 1928
 Gallart, C., Aparicio, A., Bertelli, G., & Chiosi, C. 1996b, *AJ*, 112, 2596
 Galliano, F., Madden, S. C., Jones, A. P., Wilson, C. D., Bernard, J.-P., & Le Peintre, F. 2003, *A&A*, 407, 159
 Galliano, F., Madden, S. C., Jones, A. P., Wilson, C. D., & Bernard, J.-P. 2005, *A&A*, 434, 867
 Gordon, K.D., et al. 2005, *PASP*, 177, 503
 Helou, G., Soifer, B. T., & Rowan-Robinson, M. 1985, *ApJ*, 298, L7
 Helou, G., et al. 2004, *ApJS*, 154, 253
 Hildebrand, R. H. 1983, *QJRAS*, 24, 267
 Hodge, P., Lee, M. G., & Kennicutt, R. C. 1988, *PASP*, 100, 917
 Hodge, P., Lee, M. G., & Kennicutt, R. C. 1989, *PASP*, 101, 32
 Hubble, E. P. 1925, *ApJ*, 62, 409
 Hunter, D. A., Gallagher, J. S., Rice, W. L., & Gillett, F. C. 1989, *ApJ*, 336, 152
 Hunter, D. A., et al. 2001, *ApJ*, 553, 121
 Israel, F. P. 1997, *A&A*, 317, 65
 Israel, F. P., Bontekoe, T. R., & Kester, D. J. M. 1996, *A&A*, 308, 723
 Jarrett, T. H., Chester, T., Cutri, R., Schneider, S. E., & Huchra, J. P. 2003, *AJ*, 125, 525
 Kennicutt, R. C. 1998, *ApJ*, 498, 541
 Kennicutt, R. C., et al. 2003, *PASP*, 115, 928
 Klein, U., Gr ave, R., & Wielebinski, R. 1983, *A&A*, 117, 332
 Klein, U., & Gr ave, R. 1986, *A&A*, 161, 155
 Kwan, J., & Xie, S. 1992, *ApJ*, 398, 105
 Lee, H., Skillman, E. D., & Venn, K. 2006a, *ApJ*, 642, 813
 Lee, H., Skillman, E. D., Cannon, J. M., Jackson, D. C., Gehrz, R. D., Polomski, E. F., & Woodward, C. E. *ApJ*, 647, 970
 Leroy, A., Bolatto, A. D., Simon, J. D., & Blitz, L. 2005, *ApJ*, 625, 763
 Li, A., & Draine, B. T. 2001, *ApJ*, 554, 778
 Li, A., & Draine, B. T. 2002, *ApJ*, 576, 762
 Li, A. 2004, *Penetrating Bars Through Masks of Cosmic Dust*, 535
 Lisenfeld, U., & Ferrara, A. 1998, *ApJ*, 496, 145
 Madden, S. C. 2002, *Ap&SS*, 281, 247
 Maloney, P., & Black, J. H. 1988, *ApJ*, 325, 389
 Mateo, M. L. 1998, *ARA&A*, 36, 435
 Murphy, E. J., et al. 2006a, *ApJ*, 638, 157
 Murphy, E. J., et al. 2006b, *ApJ*, submitted
 Popescu, C. C., Tuffs, R. J., V olk, H. J., Pierini, D., & Madore, B. F. 2002, *ApJ*, 567, 221
 Regan, M. W., et al. 2004, *ApJS*, 154, 204
 Rieke, G. H., et al. 2004, *ApJS*, 154, 25
 Roussel, H., et al. 2006, *ApJ*, 646, 841
 Schlegel, D. J., Finkbeiner, D. P., & Davis, M. 1998, *ApJ*, 500, 525
 Skillman, E. D., Terlevich, R., & Melnick, J. 1989, *MNRAS*, 240, 563
 Sodroski, T. J., Odegard, N., Arendt, R. G., Dwek, E., Weiland, J. L., Hauser, M. G., & Kelsall, T. 1997, *ApJ*, 480, 173
 Taylor, C. L., Kobulnicky, H. A., & Skillman, E. D. 1998, *AJ*, 116, 2746
 Thronson, H. A., Jr., & Telesco, C. M. 1986, *ApJ*, 311, 98
 Weldrake, D. T. F., de Blok, W. J. G., & Walter, F. 2003, *MNRAS*, 340, 12
 Werner, M. W., et al. 2004, *ApJS*, 154, 1
 Wyder, T. K. 2001, *AJ*, 122, 2490
 Wyder, T. K. 2003, *AJ*, 125, 3097